# Geometric Solutions for Problems in Velocity-Based Orbit Determination

Courtney L. Hollenberg[1] · John A. Christian[1] 🆔

## Abstract

Classical techniques for initial orbit determination (IOD) require the analyst to find a body's orbit given only observations such as bearings, range, and/or position. In these cases, one of the goals is often to solve for the unknown velocity vector at one or more of the observation times to fully define the orbit. Recently, however, a new class of IOD problems has been proposed that switches the knowns and unknowns in these classic IOD problems. Specifically, the objective is to find the unknown position vectors given only velocity measurements. This paper presents a detailed assessment of the geometric properties of this new family of velocity-only IOD problems. The primary tool for this geometric analysis is Hamilton's orbital hodograph, which is known to be a perfect circle for all orbits obeying Keplerian dynamics. This framework is used to produce intuitive and efficient algorithms for IOD from three velocity vectors (similar structure to Gibbs problem) and for IOD from two velocity vectors and time-of-flight (similar structure to Lambert's problem). Performance of these algorithms is demonstrated through numerical results.

**Keywords** Orbit determination · Hodograph · Velocity-Only IOD · Orbital geometry

## Introduction

Determining the orbits of planets, moons, comets, and asteroids from limited observations was the motivating problem for much of the classical work in astrodynamics. We often refer to this problem as initial orbit determination (IOD), defined here as estimating the orbit of a body given a set of measurements and with no a-priori

✉ John A. Christian
  chrisj9@rpi.edu

  Courtney L. Hollenberg
  hollec2@rpi.edu

[1] Department of Mechanical, Aerospace, and Nuclear Engineering, Rensselaer Polytechnic Institute, Troy, NY 12180, USA

information about the orbit itself. The type and quantity of available observations has naturally led to a few families of IOD problems, with each having accumulated a number of solutions over centuries of study.

For much of human history, observations of bodies in our solar system came exclusively from ground-based instruments (often telescopes after their popularization in the early 1600s [18]). As a consequence, all we had to work with for orbit determination were bearings to these bodies, which in turn led to IOD problems based on angles and positions. A brief summary of the fascinating history of IOD from such measurements may be found on pp. 419-422 of [24].

The nature of our historical methods for observing objects in our solar system gave rise to the classical families of IOD problems seen in most textbooks today. These include solving the IOD problem given: 1. three bearing measurements at known times (angles-only IOD; e.g., methods of Gauss, Laplace, Gooding), 2. three position measurements (Gibbs problem), or 3. two position measurements and time-of-flight (Lambert's problem). Other less standard IOD problems are routinely investigated and solved (e.g., [19]), although nearly all assume some of the known information to be related to position (e.g., bearings, range, position). Solution methods to all these problems abound in the literature [4, 5, 12, 14, 19, 21, 24], and their detailed study is left to the reader.

New sensing technologies, however, motivate the consideration of a completely new class of IOD problems. In a recent paper [9], we posed the novel problem of IOD when only velocity vectors are known (meaning we must solve for the unknown position vectors). The consideration of velocity-only IOD was originally inspired by X-ray navigation (XNAV) [22], which can produce inertial velocity measurements without any positioning information [9]. The same idea works with any other sensor capable of producing inertial velocity measurements that may become available in the future.

In hindsight, velocity-only IOD seems like a rather obvious inversion of the classic IOD problems. For example, estimating the orbit from three velocity vectors is similar in structure to the Gibbs problem, but where the knowns and unknowns have been switched (specifically, the Gibbs problem has known positions and unknown velocities, while our problem has known velocities and unknown positions). Likewise, estimating the orbit from two velocity vectors and time-of-flight (TOF) is similar in problem structure to Lambert's problem. The parallel structure is discussed at length in [9]. Before proceeding further, however, we feel it important to stress that the current work is not an alternative to the Gibbs or Lambert problem since the measurements are fundamentally different (velocity vs. position). Instead, we simply have a novel IOD problem with a structure that is reminiscent of these classical IOD methods.

In this work, we expand on our earlier work from [9] in a few important ways. First, we consider the geometry of the velocity-only IOD problem through the use of the orbital hodograph [3], leading to a number of important and novel insights. Second, we use the hodograph to develop a new solution to IOD from three or more velocity vectors and compare the result to our original method from [9]. Third, we provide the first known solution to the problem of IOD from two velocity vectors and time-of-flight.

## Background

The geometric solution to the velocity-only IOD problem investigated in this work is based on the orbital hodograph. The hodograph, first proposed by Hamilton in 1847 [17], is the curve traced out by a trajectory's velocity vector — that is, the locus of points formed by the tip of the changing velocity vector while keeping the tail of the vector fixed (usually at the origin). The hodograph is a circle for every two-body orbit, making it a useful tool to arrive at elegant geometric solutions for many problems in astrodynamics.

Detailed studies of the orbital hodograph and its application to modern space-flight were undertaken at least as early as the 1960s [3, 11]. Despite this history and its practical utility in solving a variety of problems (e.g., [2, 8, 13, 23]), the hodograph remains a relatively obscure tool throughout much of the astrodynamics community — receiving only passing mention (at best) in most modern astrodynamics texts (e.g., [5]). Indeed, its obscurity has led to its repeated "rediscovery" (always with much excitement) over the last half century [10]. The hodograph approach is also periodically adopted and championed by advocates, most recently becoming popular through the publication of *Feynman's Lost Lecture* [15] and how it can be used to teach orbital mechanics without calculus [7, 16]. Here, we are not claiming (re)discovery of the circular hodograph for Keplerian orbits, but rather applying this tool to a problem for which it is especially well-suited.

For an object undergoing simple two-body motion, the hodograph will always be a perfect circle — regardless of if the orbit itself is circular, elliptical, parabolic, or hyperbolic. This fascinating property of conic orbits is straightforward to prove (see Appendix A.1 or [6]) and was discovered by Hamilton in his original work on the hodograph from 1847 [17]. The circular nature of the orbital hodograph is illustrated for an example elliptical orbit in Fig. 1, where the orbit is shown on the left and the hodograph on the right.

Interestingly, the classical orbital hodograph from Fig. 1 may also be plotted in the rotating local-vertical local-horizontal (LVLH) frame and retain its circular shape. Further, if this version of the orbital hodograph is scaled by $h/\mu$, the result is a circle whose radius is the orbit eccentricity and whose center is located at coordinates [1,0] in the rotating frame. This geometry is illustrated in Figs. 2 and 3. It is this scaled and rotated version of the hodograph that many modern aerospace practitioners are most familiar with — largely due to the brief hodograph discussion on pp. 126–128 of Battin's classic text on astrodynamics [5].

While the geometry of the rotating orbital hodograph (Figs. 2 and 3) is important and helps define a few critical variables (e.g., the unit vectors of the LVLH frame, $u_\parallel$ and $u_\perp$), our present discussion primarily makes use of the classic (non-rotating) orbital hodograph from Fig. 1.

## Problem Statement

The IOD problems discussed in this paper assume motion governed by simple Keplerian dynamics. Thus, application of Newton's universal law of gravitation leads to the
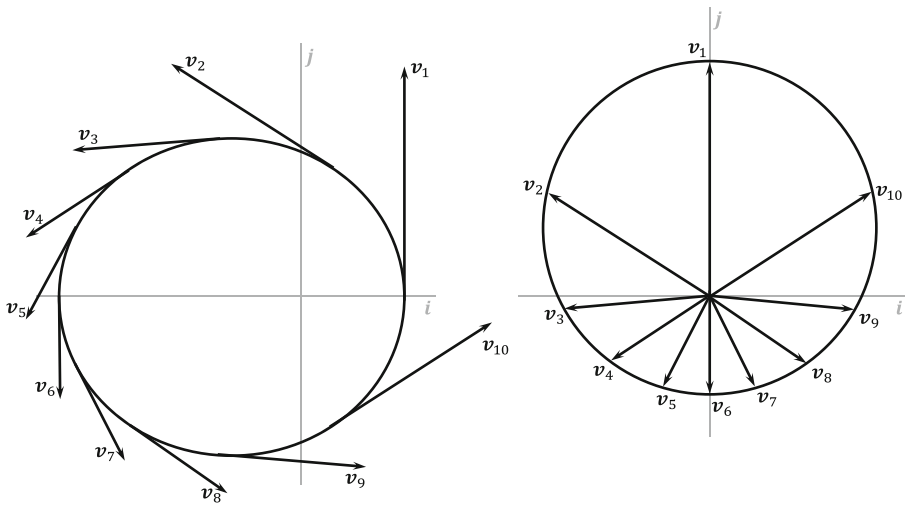
**Fig. 1** Velocity vectors on both the orbital path of a satellite (left) and its corresponding unmodified hodograph representation (right)

standard two-body equation of motion for an orbiting body (e.g., spacecraft) relative to a central body (e.g., Earth, Sun),

$$\frac{d^2}{dt^2}\boldsymbol{r} = -\frac{\mu}{\|\boldsymbol{r}\|^3}\boldsymbol{r} \tag{1}$$

where $\boldsymbol{r} \in \mathbb{R}^3$ is the position vector of the orbiting body relative to the central body, and $\mu$ is the central body's gravitational parameter. The trajectory of the orbiting body is uniquely determined by the Cartesian state vectors $\boldsymbol{r}_i$ and $\boldsymbol{v}_i$ at time $t_i$. The
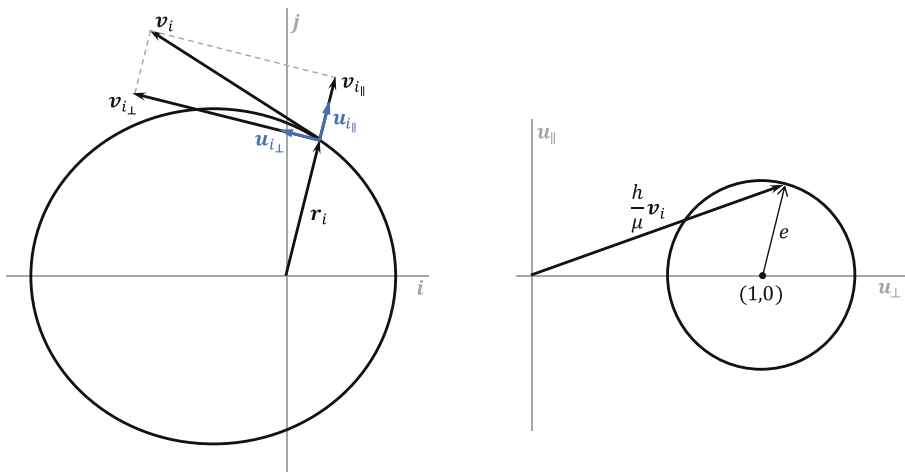


**Fig. 2** Velocity vector decomposed into its LVLH components shown on the orbit (left) and modified hodograph (right)
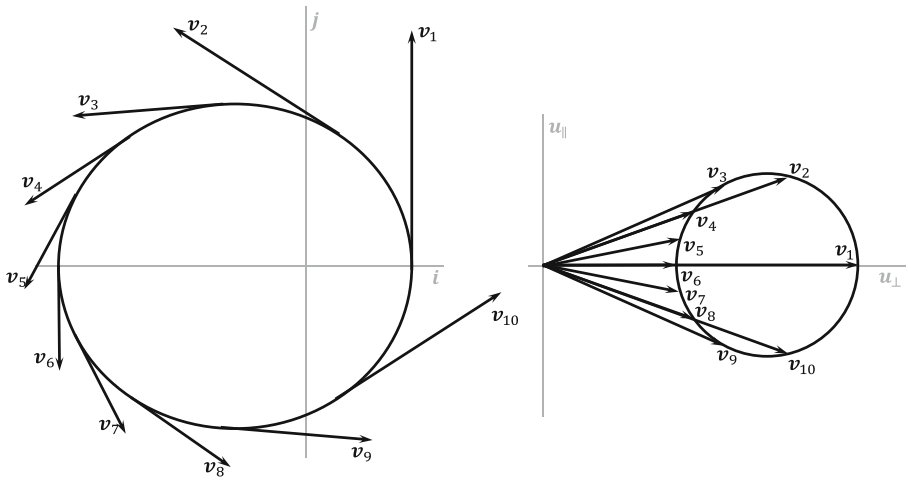
**Fig. 3** Multiple velocity vectors on the orbital path of a satellite (left) and the modified hodograph representation in the LVLH frame (right)

problem statements for the two new methods of IOD are presented in the following paragraphs, and a graphical depiction can be seen in Fig. 4.

The first problem is analogous in structure to the Gibbs problem of IOD from three position vectors. Given the central body's gravitational parameter ($\mu$), the direction of motion, and three velocity vectors $\{v_1, v_2, v_3\}$, determine at least one of the unknown position vectors in $\{r_1, r_2, r_3\}$. This same problem may be generalized to the set of $n$ velocity vectors $\{v_1, v_2, ..., v_n \mid n \geq 3\}$.

The second problem is analogous in structure to Lambert's problem of IOD from two position vectors and time-of-flight. Given the central body's gravitational parameter ($\mu$), the direction of motion, the velocity vectors at two different times ($v_1$ and $v_2$), the time between them ($\Delta t$), and the number of revolutions about the central body ($N$), determine one (or both) of the unknown position vectors $r_1$ and/or $r_2$. This is a two-point boundary value problem (TPBVP).
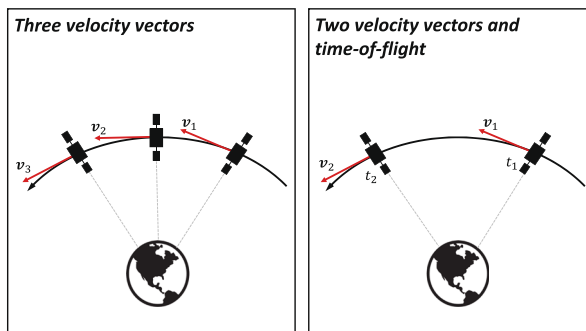


**Fig. 4** Graphical depiction of the IOD problems to which solutions are presented

## Analytic Solution to IOD Problem Given Three or More Velocity Vectors

The solution to the velocity-only IOD problem can be computed analytically when three or more velocity vectors are given. The first known solution to this problem was presented in [9]. Here, we develop a new solution based on the geometry of the orbital hodograph. Our new solution process is broken up into three basic steps: hodograph fit, orbit shape determination, and orbit scale determination.

### Hodograph Fit

Recall that the tips of the velocity vectors belonging to a two-body orbit trace out a circle, regardless of the orbit type. This circle is the orbital hodograph. Therefore, the first step in the IOD problem is to find the hodograph by fitting a circle to the velocity vectors. This is usually a well-posed problem, since a circle is uniquely defined for three (or more) generally placed points. Thus, the requirement for a unique IOD solution is simply that there are at least three different velocity vectors. While there are a number of circle-fitting methods that can be used to determine the hodograph, we choose to solve this problem by computing a two-dimensional circle fit on the projection of the velocity vectors onto the orbit plane.

Two-body orbits are planar, meaning all velocity vectors (as well as position vectors) must lie in the same plane. This plane, which is defined by its unit normal $\boldsymbol{k}$, is defined using the same method presented in [9]. Since the velocity vectors must all lie within the orbital plane, we know that $\boldsymbol{v}_i^T \boldsymbol{k} \approx 0$. Thus, we can find the solution for $\boldsymbol{k}$ as the one-dimensional null-space of the $n \times 3$ matrix

$$
\boldsymbol{N} = \begin{bmatrix} \boldsymbol{v}_1^T \\ \boldsymbol{v}_2^T \\ \vdots \\ \boldsymbol{v}_n^T \end{bmatrix}
\tag{2}
$$

The null space is found in the total least-squares (TLS) sense through the singular value decomposition (SVD) $\boldsymbol{N} = \boldsymbol{U}\boldsymbol{D}\boldsymbol{V}^T$. The unit normal $\boldsymbol{k}$ is given by the column of $\boldsymbol{V}$ corresponding to the smallest singular value in $\boldsymbol{D}$. The direction of $\boldsymbol{k}$ is chosen to be in the same direction of the orbit's specific angular momentum, $\boldsymbol{h}$, such that $\boldsymbol{h} = h\boldsymbol{k}$, where $h = \|\boldsymbol{h}\|$. This convention is achieved using one of the three techniques in [9].

The two-dimensional hodograph circle can now be fit within this plane. Thus, proceed by transforming the velocity vectors $\{\boldsymbol{v}_i\}_{i=1}^n$ from their original (and presumably inertial) frame to a new orbit frame whose $z$-axis is in the direction of $\boldsymbol{k}$,

$$
\begin{bmatrix} \dot{x}_{O_i} \\ \dot{y}_{O_i} \\ \dot{z}_{O_i} \end{bmatrix} = \boldsymbol{T}_O^I \boldsymbol{v}_i
\tag{3}
$$

where $\boldsymbol{T}_O^I$ is the rotation matrix from the inertial frame to the orbit frame.

Without loss of generality, let the $x$-direction of the orbit frame be perpendicular to both $\boldsymbol{v}_1$ and $\boldsymbol{k}$

$$\boldsymbol{u}_x = \frac{\boldsymbol{v}_1 \times \boldsymbol{k}}{\|\boldsymbol{v}_1 \times \boldsymbol{k}\|} \tag{4}$$

and let $\boldsymbol{u}_y$ complete the right-handed system $\{\boldsymbol{u}_x, \boldsymbol{u}_y, \boldsymbol{k}\}$. Therefore, the rotation matrix $\boldsymbol{T}_O^I$ is given by

$$\boldsymbol{T}_O^I = \begin{bmatrix} \boldsymbol{u}_x^T \\ \boldsymbol{u}_y^T \\ \boldsymbol{k}^T \end{bmatrix} \tag{5}$$

Since the orbit is planar, the $z$-component of velocity should be zero when expressed in the orbital frame,

$$\begin{aligned} \dot{z}_{O_i} &= 0 & \forall i & \quad \text{(noise free)} \\ \dot{z}_{O_i} &= \epsilon_i \approx 0 & \forall i & \quad \text{(noisy)} \end{aligned} \tag{6}$$

Assuming an orthographic projection onto the $\boldsymbol{u}_x$-$\boldsymbol{u}_y$ plane, the $z$-component of the velocity vectors in the orbit frame is simply ignored in the two-dimensional hodograph fit. Only $\{\dot{x}_{O_i}\}_{i=1}^n$ and $\{\dot{y}_{O_i}\}_{i=1}^n$ are used.

Therefore, given the measurements $\{\dot{x}_{O_i}, \dot{y}_{O_i}\}_{i=1}^n$, the fit of the hodograph in the orbit plane is performed using the equation of a circle

$$\left(\dot{x}_{O_i} - \dot{x}_c\right)^2 + \left(\dot{y}_{O_i} - \dot{y}_c\right)^2 = R^2 \tag{7}$$

where $(\dot{x}_c, \dot{y}_c)$ are the two-dimensional coordinates of the hodograph circle center in the orbit frame and $R$ is the radius of the hodograph circle.

Our desire to obtain a fast and non-iterative solution leads us to construct a best-fit circle that minimizes algebraic distance (instead of geometric distance) between the measured points and the circle. The approach used here is consistent with well-established methods for algebraic circle fitting [1]. Therefore, expanding Eq. 7 and letting

$$g = \dot{x}_c^2 + \dot{y}_c^2 - R^2 \tag{8}$$

results in the following linear system

$$\begin{bmatrix} 2\dot{x}_{O_1} & 2\dot{y}_{O_1} & -1 \\ 2\dot{x}_{O_2} & 2\dot{y}_{O_2} & -1 \\ \vdots & \vdots & \vdots \\ 2\dot{x}_{O_n} & 2\dot{y}_{O_n} & -1 \end{bmatrix} \begin{bmatrix} \dot{x}_c \\ \dot{y}_c \\ g \end{bmatrix} = \begin{bmatrix} \dot{x}_{O_1}^2 + \dot{y}_{O_1}^2 \\ \dot{x}_{O_2}^2 + \dot{y}_{O_2}^2 \\ \vdots \\ \dot{x}_{O_n}^2 + \dot{y}_{O_n}^2 \end{bmatrix} \tag{9}$$

This system can be solved in the least-squares sense for $\dot{x}_c$, $\dot{y}_c$, and $g$ for any set of $n \geq 3$ velocity measurements in a non-degenerate configuration. The scalar value $R$ representing the hodograph radius can then be computed from Eq. 8 as

$$R = \sqrt{\dot{x}_c^2 + \dot{y}_c^2 - g} \tag{10}$$

The three-dimensional coordinates of the hodograph circle center expressed in the inertial frame are found from

$$\boldsymbol{c} = \left[\boldsymbol{T}_O^I\right]^T \begin{bmatrix} \dot{x}_c \\ \dot{y}_c \\ 0 \end{bmatrix} \tag{11}$$

## Orbit Shape Determination

All the details of the orbit shape are encoded in the location of the hodograph center, $c$, and its radius, $R$. Observe that, with the exception of a circular orbit, the center of the hodograph is offset from the origin. Consequently, the magnitude of the velocity vector changes as one goes around the hodograph circle. Since an orbit's speed is greatest at periapsis, the periapsis velocity vector, $\boldsymbol{v}_p$, must be pointing in the direction from the origin to the circle center (because, as can be seen in Fig. 5, the direction of $\boldsymbol{c}$ always corresponds to the direction on the hodograph furthest from the origin). In the case of an elliptical orbit, similar logic shows that the apoapsis velocity vector, $\boldsymbol{v}_a$, must point away from the circle center.

This geometry leads to straightforward relations between the velocity magnitude (speed) at periapsis, $v_p = \|\boldsymbol{v}_p\|$, the velocity magnitude (speed) at apoapsis, $v_a = \|\boldsymbol{v}_a\|$, and the hodograph parameters $c$ and $R$:

$$v_p = R + c \tag{12}$$

$$v_a = R - c \tag{13}$$

where $c = \|\boldsymbol{c}\|$.

From the conservation of specific angular momentum,

$$\begin{aligned} h &= \|\boldsymbol{r} \times \boldsymbol{v}\| \\ &= r_a v_a = a(1 + e)v_a \\ &= r_p v_p = a(1 - e)v_p \end{aligned} \tag{14}$$

which may be rearranged to find the orbit eccentricity as a function of the speeds at apoapsis and periapsis

$$e = \frac{v_p - v_a}{v_p + v_a} \tag{15}$$

which reduces to the following simple ratio
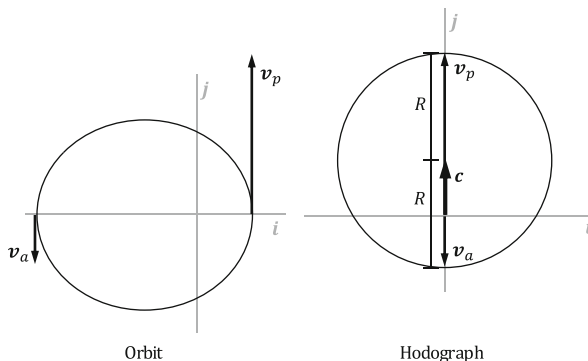
$$e = \frac{c}{R} \tag{16}$$



**Fig. 5** Apside velocities expressed in relation to the hodograph geometry. This is a visual representation of Eqs. 12 and 13

While the derivation presented here assumes an elliptical orbit, this same relationship ($e = c/R$) holds for all conic sections. The generic derivation (valid for all Keplerian orbit types) is provided in Appendix A.4, although we find it to be less geometrically insightful.

Figure 6 demonstrates the relationship in Eq. 16 for the four conic sections: circle, ellipse, parabola, and hyperbola. Note that the hodograph is a circular arc, rather than a full circle, for hyperbolic orbits. The unreachable part of the hodograph circle, described by $\theta_{\lim}$, can be analytically found for any value of $c$ and $R$ using the geometry discussed in Appendix B. In brief, a full circle is not possible for a hyperbolic orbit since the orbital speed cannot drop below the magnitude of the hyperbolic excess velocity, $\|v_\infty\|$.

With the orbit eccentricity known, we next determine the eccentricity vector. As before, this may be done through geometry. Recalling that the velocity is perpendicular to the position vector at both periapsis and apoapsis, it follows that the orbit line of apsides must be perpendicular to the vector $c$ (since, as shown in Fig. 5, the vector $c$ is collinear to the periapsis and apoapsis velocity vectors).

The eccentricity vector, $e$, lies along the line of apsides, points towards periapsis, and has a magnitude of $e$. Since $e$ lies in the orbital plane, it must also be perpendicular to the orbit unit normal, $k$. Therefore, defining the direction from the central body to the orbit periapsis as

$$u_e = \frac{c}{c} \times k \tag{17}$$



Circular ($e = 0$)    Elliptical ($0 < e < 1$)    Parabolic ($e = 1$)    Hyperbolic ($e > 1$)
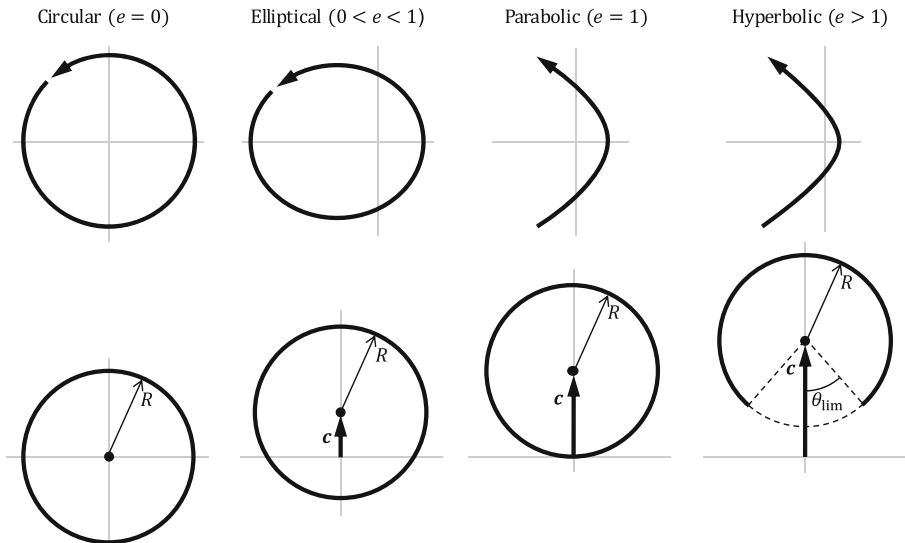
**Fig. 6** Example notional orbits (top) are shown with their corresponding hodograph (bottom). For a constant radius hodograph, the orbit eccentricity increases as the hodograph circle center moves away from the origin

it follows that the eccentricity vector is given by

$$\boldsymbol{e} = e\boldsymbol{u}_e = \frac{\boldsymbol{c}}{R} \times \boldsymbol{k} \tag{18}$$

We observe that Eqs. 17 and 18 have trouble when $\boldsymbol{c}$ is exactly at the origin, $\boldsymbol{c} = \mathbf{0}_{3\times1}$. Fortunately, we may bypass Eqs. 17 and 18 altogether when $c = 0$ since this is known to specify a circular orbit. Specifically, we observe that if $c = 0$ then $\|\boldsymbol{v}\| = R$ everywhere on the hodograph. The only way to have a constant speed everywhere on the orbit is to have a circular orbit. Thus $c = 0$ implies that $e = 0$ and, consequently, $\boldsymbol{e} = \mathbf{v}_{3\times1}$. The direction to periapsis, $\boldsymbol{u}_e$, is not defined for a circular orbit (i.e., when $c = 0$).

The final necessary piece of information about the orbit geometry that can be derived from the hodograph is the direction from the central body to the orbiting object at any given time $t_i$, denoted $\boldsymbol{u}_{\|_i}$ (see Fig. 2). This unit vector is perpendicular to the unit vector $\boldsymbol{u}_{\perp_i}$ which points from the circle center to the tip of the velocity vector

$$\boldsymbol{u}_{\perp_i} = \frac{\boldsymbol{v}_i - \boldsymbol{c}}{\|\boldsymbol{v}_i - \boldsymbol{c}\|} \tag{19}$$

such that

$$\boldsymbol{u}_{\|_i} = \boldsymbol{u}_{\perp_i} \times \boldsymbol{k} = \frac{\boldsymbol{v}_i - \boldsymbol{c}}{\|\boldsymbol{v}_i - \boldsymbol{c}\|} \times \boldsymbol{k} \tag{20}$$

The geometric relationship in Eq. 20 is illustrated in Fig. 7. For those unfamiliar with why this is the case, key hodograph geometric relations are derived in Appendix A.

## Orbit Size Determination

The last step in the solution method is to determine the size of the orbit by solving for range, $\rho_i$. Orbit size determination requires consideration of the integrals of motion.

Begin with the equation for specific angular momentum

$$\boldsymbol{h} = \boldsymbol{r}_i \times \boldsymbol{v}_i = \left(\rho_i \boldsymbol{u}_{\|_i}\right) \times \boldsymbol{v}_i \tag{21}$$

Recall that $\boldsymbol{k}$ was defined to be in the same direction as $\boldsymbol{h}$, so that Eq. 21 may be written as

$$\boldsymbol{h} = h\boldsymbol{k} = \rho_i \|\boldsymbol{v}_{\perp_i}\| \boldsymbol{k} \tag{22}$$
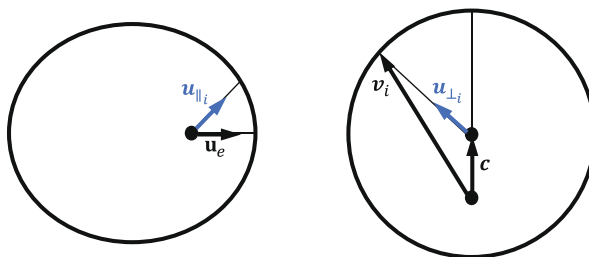


**Fig. 7** The unit vector from the hodograph center to the velocity vector tip, $\boldsymbol{u}_{\perp_i}$ (blue, right), is perpendicular to the unit vector from the central body to the orbiting body at time $t_i$, $\boldsymbol{u}_{\|_i}$ (blue, left). The vector from the hodograph origin to the circle center, $\boldsymbol{c}$ (right), is perpendicular to the orbit eccentricity vector direction $\boldsymbol{u}_e$ (left)

where $\boldsymbol{v}_{\perp_i}$ is the component of velocity perpendicular to the radius (see Fig. 2), which is given by the projection of the velocity vector onto $\boldsymbol{u}_{\perp_i}$

$$\boldsymbol{v}_{\perp_i} = \left(\boldsymbol{u}_{\perp_i}^T \boldsymbol{v}_i\right)\boldsymbol{u}_{\perp_i} = \left(\boldsymbol{u}_{\perp_i}\boldsymbol{u}_{\perp_i}^T\right)\boldsymbol{v}_i \tag{23}$$

This can also be written as

$$\boldsymbol{v}_{\perp_i} = \boldsymbol{v}_i - \left(\boldsymbol{u}_{\|_i}^T \boldsymbol{v}_i\right)\boldsymbol{u}_{\|_i} = \left(\boldsymbol{I}_{3\times3} - \boldsymbol{u}_{\|_i}\boldsymbol{u}_{\|_i}^T\right)\boldsymbol{v}_i \tag{24}$$

Continue with the equation for the eccentricity vector given by

$$\mu\boldsymbol{e} = \boldsymbol{v}_i \times \boldsymbol{h} - \frac{\mu}{\rho_i}\boldsymbol{r}_i = \boldsymbol{v}_i \times \boldsymbol{h} - \mu\boldsymbol{u}_{\|_i} \tag{25}$$

Substituting Eqs. 22 into 25 gives

$$\mu\boldsymbol{e} = \boldsymbol{v}_i \times \left(\rho_i\|\boldsymbol{v}_{\perp_i}\|\boldsymbol{k}\right) - \mu\boldsymbol{u}_{\|_i} \tag{26}$$

which can be rewritten as

$$\mu\left(\boldsymbol{e} + \boldsymbol{u}_{\|_i}\right) = \rho_i\|\boldsymbol{v}_{\perp_i}\|\left(\boldsymbol{v}_i \times \boldsymbol{k}\right) \tag{27}$$

Taking the magnitude of both sides results in

$$\mu\left\|\boldsymbol{e} + \boldsymbol{u}_{\|_i}\right\| = \rho_i\|\boldsymbol{v}_{\perp_i}\|\|\boldsymbol{v}_i\| \tag{28}$$

where, since $\boldsymbol{k}$ is a unit vector which is orthogonal to $\boldsymbol{v}_i$, $\|\boldsymbol{v}_i \times \boldsymbol{k}\| = \|\boldsymbol{v}_i\|$.

Finally, solve for $\rho_i$

$$\rho_i = \frac{\mu\left\|\boldsymbol{e} + \boldsymbol{u}_{\|_i}\right\|}{\|\boldsymbol{v}_{\perp_i}\|\|\boldsymbol{v}_i\|} \tag{29}$$

and compute the full position vector as

$$\boldsymbol{r}_i = \rho_i\boldsymbol{u}_{\|_i} \tag{30}$$

### Algorithm Summary

A brief summary outlining the solution procedure for performing IOD with three or more velocity vectors is provided in Table 1.

## Iterative Solution to IOD Problem Given Two Velocity Vectors and Time-of-Flight

The hodograph geometry may also be used to solve the problem of IOD given two velocity vectors, $\boldsymbol{v}_1$ and $\boldsymbol{v}_2$, and time-of-flight (TOF), $\Delta t = t_2 - t_1$. Like Lambert's Problem, this problem is a TPBVP for Keplerian dynamics and requires an iterative method to meet both endpoint constraints. While studies of the properties of the terminal velocity vectors for the orbital boundary problem exist (most notably Sections 6.1 and 6.8 of [5]), these properties are usually not discussed within the context of IOD.

Unlike in the first IOD problem, where three or more velocity measurements uniquely define the orbital hodograph circle, there are an infinite number of circles

**Table 1** Algorithm summary for IOD from three velocity vectors

| | |
|---|---|
| Step 1: | Obtain three (or more) velocity vector measurements $\{v_1, v_2, ..., v_n\}$ and specify the direction of motion. |
| Step 2: | Compute the orbital plane normal vector, $k$, by the SVD of $N$ from Eq. 2 with direction chosen according to the direction of motion. |
| Step 3: | Transform the velocity vectors into two-dimensional coordinates using Eq. 3. |
| Step 4: | Complete the two-dimensional circle fit by solving the linear system given in Eq. 9 to find $\dot{x}_c$ and $\dot{y}_c$. Compute $R$ from Eq. 10. |
| Step 5: | Transform the solution back into the three-dimensional inertial frame to get $c$ with Eq. 11. |
| Step 6: | Compute the eccentricity vector, $e$, from Eq. 18. |
| Step 7: | Find the direction for each measurement $u_{\|i}$ using Eq. 20. |
| Step 8: | Compute $\rho_i$ using Eq. 29. |
| Step 9: | Compute $r_i$ using Eq. 30. |
| Step 10: | Having found inertial position vectors at any of the given measurement times, the IOD problem is complete. |

that can be fit to the two given velocity measurements. As a consequence, geometry alone cannot be used to perform IOD with two velocity vectors. However, the family of possible hodograph circles passing through the two velocity vectors are constrained by a one-dimensional parameterization, with each circle having a different time-of-flight between the two measurement times. The circle producing the desired TOF is the hodograph we seek.

Since the hodograph is a circle, it is clear that the hodograph's center must be equidistant from the vector tips and must therefore lie on the perpendicular bisector of the segment joining the two vector tips. In three-dimensional space, the perpendicular bisector is a plane, but the search for the hodograph center is restricted to the line formed by the intersection of the perpendicular bisector's plane with the orbital plane. A graphical depiction of some possible hodograph fits given two velocity vectors is shown in Fig. 8. Observe the variation in orbit eccentricity, line of apsides, and size as the hodograph centerpoint moves along the perpendicular bisector.

## Parameterization

Again, the first step is to define the orbital plane by its normal vector using the same convention as before

$$k = \pm \frac{v_1 \times v_2}{\|v_1 \times v_2\|} \tag{31}$$

where the sign is chosen according to the direction of motion: $h = hk$. Clearly, $v_1$ and $v_2$ may not be collinear if the orbital plane is to be uniquely defined.

Next, we define the line describing the perpendicular bisector using a one-dimensional parameterization in $s_k$,
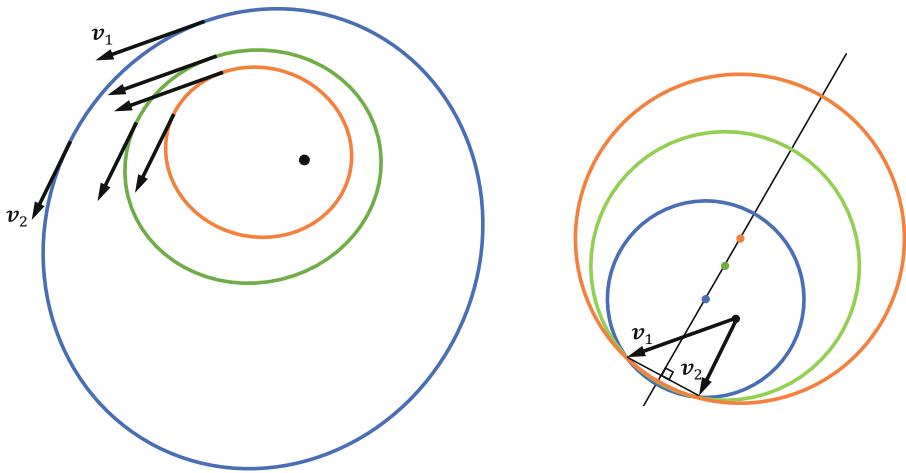
$$c_k = s_k m + b \tag{32}$$

**Fig. 8** Example possible hodograph fits (right) from two velocity vectors are shown with their corresponding color-coded orbits (left)

where $b$ is a known point on the line and the unit vector $m$ is its direction.

By definition, the perpendicular bisector must contain the midpoint between the two velocity measurements. We choose this point to be $b$ in the above parameterization

$$b = \frac{v_1 + v_2}{2} \tag{33}$$

The direction of the perpendicular bisector is orthogonal to the vector connecting the two velocity measurements, $v_2 - v_1$, as well as the plane normal $k$ so that

$$m = \pm \frac{(v_2 - v_1) \times k}{\|(v_2 - v_1) \times k\|} \tag{34}$$

where the sign is chosen such that $b^T m > 0$.

A graphical depiction of the one-dimensional hodograph parameterization is shown in Fig. 9.

The radius of any hodograph circle is then given by

$$R_k = \|v_i - c_k\| \tag{35}$$

## Feasible Region for Hodograph Parameter $s$

In most cases, the time-of-flight as a function of the hodograph parameter $s_k$ monotonically increases and asymptotically approaches infinity in one of two places: 1. at a parabolic orbit (when the data only permit a closed orbit) or 2. where the minimum of the two velocity vectors becomes the two velocity vectors becomes the hyperbolic excess velocity (when the data permit an open orbit). These conditions create an upper bound on the physically realizable value of the parameter $s_k$, with the limiting value being denoted as $s_{\text{lim}}$.
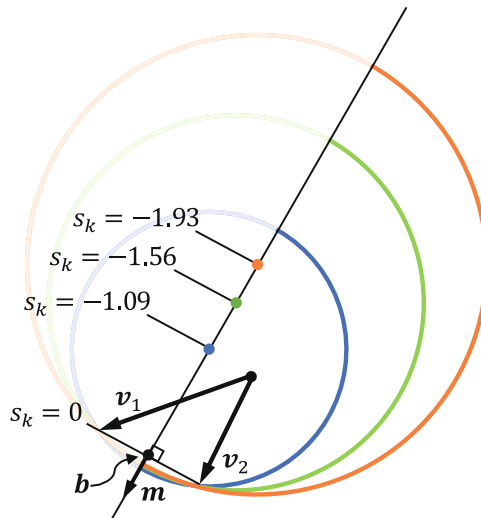
**Fig. 9** Graphical depiction of parameterized perpendicular bisector along which all possible hodograph centerpoints lie

The first limiting case occurs when an open orbit is not possible for the given set of velocity vectors. Recall that the direction of $k$ was determined based on the direction of motion using the same convention as [9]. Because there can never be more than 180 deg of separation between velocity vectors in an open orbit, $v_1 \times v_2$ for an ordered set of measurements $\{v_1, v_2\}$ must be in the direction $k$ for an open orbit to be possible. Additionally, multiple revolutions are not possible for open orbits (it is not possible to have $N \geq 1$, where $N$ is the number of full revolutions).

Therefore, an open orbit is not possible when either $N \geq 1$ or $(v_1 \times v_2)^T k < 0$. If either is true, the value of $s_k$ may not exceed that of a parabolic orbit, $s_{par}$. This occurs when the hodograph circle passes through the origin, $O$, at $[0, 0]$. Therefore, compute $c_{par}$ by fitting a circle to the three points $v_1$, $v_2$, and $O$ in the orbit plane. This can be done using Eqs. 3–11. The maximum parameter value, $s_{lim}$, is then simply

$$s_{lim} = s_{par} = \frac{c_{par_j} - b_j}{m_j} \quad \text{when } (v_1 \times v_2)^T k < 0 \quad \lor \quad N \geq 1 \qquad (36)$$

where the subscript $j$ represents either the $x$, $y$, or $z$ coordinate of the inertial frame. We suggest choosing the $j$ to be the direction corresponding to the largest element (in magnitude) of $m$.

The second limiting case occurs when the smaller of the two velocity vectors approaches the hyperbolic excess velocity

$$v_\infty = \begin{cases} v_1, & \|v_1\| \leq \|v_2\| \\ v_2, & \|v_1\| > \|v_2\| \end{cases} \qquad (37)$$

The corresponding value of $s_{v_\infty}$ can be determined by making $v_\infty$ tangent to the hodograph circle, thus forming the right triangle shown in Fig. 31 in Appendix B. Define the radius vector as

$$R_{v_\infty} = v_\infty - c_{v_\infty} \tag{38}$$

We seek the radius $R_{v_\infty}$ such that

$$v_\infty^T R_{v_\infty} = v_\infty^T v_\infty - v_\infty^T b - s_{v_\infty} v_\infty^T m = 0 \tag{39}$$

It follows that

$$s_{\lim} = s_{v_\infty} = \frac{v_\infty^T v_\infty - v_\infty^T b}{v_\infty^T m} \quad \text{when } (v_1 \times v_2)^T k > 0 \tag{40}$$

Combining the results of Eqs. 36 and 40, the parameter upper bound, $s_{\lim}$, is

$$s_{\lim} = \begin{cases} s_{\text{par}}, & (v_1 \times v_2)^T k < 0 \quad \vee \quad N \geq 1 \\ s_{v_\infty}, & (v_1 \times v_2)^T k > 0 \end{cases} \tag{41}$$

### Determination of Transfer Time

Any selection for the parameter $s_k$ within the feasible region ($s_k < s_{\lim}$) describes a feasible orbital hodograph, and thus produces a unique, feasible, and fully defined orbit. From the hodograph formed by $s_k \to \{c_k, R_k\}$ (see Eqs. 32 and 35), we may immediately find the unknown position vectors $r_1$ and $r_2$ using the same procedure as for the three velocity vector IOD method. Specifically, this is done by applying Steps 6-9 from the algorithm in Table 1.

We now have a fully defined orbit, with the position and velocity known at two points along this orbit. The TOF from the first point to the second point may be found through the straightforward application of Kepler's equation (or its equivalent). Detailed discussions of finding the TOF between two points on a known orbit through Kepler's equation may be found in almost any astrodynamics textbook, such as [4, 5, 24].

### Uniqueness of IOD Solution

We already know from before (see Eq. 31 and discussion that follows) that an orbit cannot be uniquely defined from two collinear velocity vectors because the orbital plane cannot be uniquely defined. This parallels the difficulty associated with collinear position vectors (180 deg transfers) found in the classic Lambert's problem.

Unlike its Lambert's problem counterpart, however, a unique solution for IOD from two non-collinear velocity vectors and TOF is not always possible. There are certain geometries for the velocities $v_1$ and $v_2$ where TOF does not monotonically increase with the parameter $s_k$, thus producing multiple feasible values of $s_k$ (and, by extension, multiple different hodographs and corresponding orbits) that satisfy certain values of TOF. Interestingly, whether or not TOF monotonically increases with $s_k$ depends only on the number of revolutions about the central body ($N$), the

angle $\phi$ between $\boldsymbol{v}_1$ and $\boldsymbol{v}_2$ (measured in the direction of motion), and the ratio of the smaller speed to the larger speed ($q$):

$$q = \begin{cases} \frac{\|\boldsymbol{v}_2\|}{\|\boldsymbol{v}_1\|}, & \|\boldsymbol{v}_1\| \geq \|\boldsymbol{v}_2\| \\ \frac{\|\boldsymbol{v}_1\|}{\|\boldsymbol{v}_2\|}, & \|\boldsymbol{v}_1\| < \|\boldsymbol{v}_2\| \end{cases} \tag{42}$$

where $q \leq 1$ by construction.

The geometric regions for unique solutions ($\mathcal{A}$) and non-unique solutions ($\mathcal{B}$) are best visualized in polar coordinates as shown in Fig. 10 (where it is assumed the spacecraft has not made a full revolution about the central body, $N = 0$). We further observe that the region containing non-unique solutions is dependent on the number of revolutions, with the size of region $\mathcal{B}$ shrinking as the number of revolutions ($N$) increases. This is shown for $N = 0$ to $N = 4$ in Fig. 11.

A few things are immediately evident. First, the solution is always unique if the direction of the velocity vector turns more than 180 deg between the first and second observation. Second, it makes no difference if the larger speed is $\|\boldsymbol{v}_1\|$ or $\|\boldsymbol{v}_2\|$ in forming the ratio $q$; the consequence in terms of IOD uniqueness is the same. Third, we always know at the outset if our two velocity measurements place us in the region where non-unique solutions are possible. Fourth, uniqueness has nothing to do with the parameters of the actual orbit (e.g., type of conic section, eccentricity, inclination, semi-major axis, period). Certain combinations of $\phi$, $q$, and $N$ will always produce a range of TOFs that could be explained by multiple values of $s_k$ (and, hence, multiple
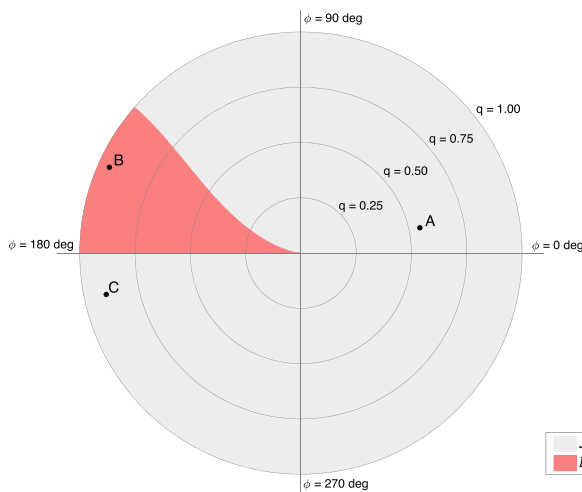


**Fig. 10** Polar plot of IOD solution uniqueness for all possible velocity pair geometries for $N = 0$, as parameterized by the angle from $\boldsymbol{v}_1$ to $\boldsymbol{v}_2$ measured in the direction of motion ($\phi$) and relative speed $q$ (Eq. 42). The light gray region ($\mathcal{A}$) represents geometries where all IOD solutions are unique. The light red region ($\mathcal{B}$) represents geometries where non-unique IOD solutions are possible and some TOFs may be explained by more than one feasible orbit. Markers A, B, and C are example velocity pair geometries used to illustrate properties of the two-velocity IOD problem in Figs. 12–15
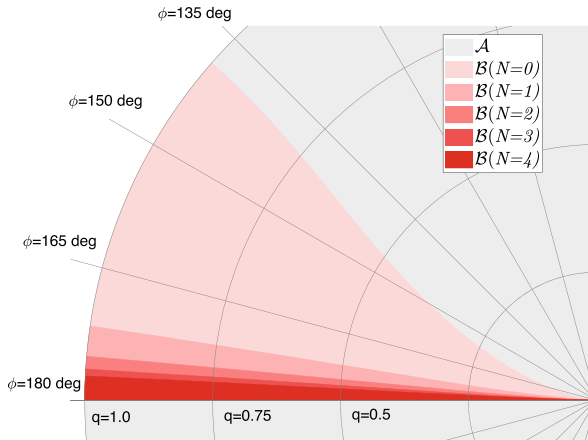
**Fig. 11** Polar plot of IOD solution uniqueness for all possible velocity pair geometries as the number of revolutions about the central body increases from $N = 0$ to $N = 4$. Conventions are identical to that of Fig. 10. The light red region $\mathcal{B}(N = 0)$ in this figure is identical to the light red region in Fig. 10. Observe that the region where non-unique geometries may exist shrinks as the number of revolutions increases

orbits). As a consequence, even along the same orbit it is common for some measurement combinations to produce unique TOFs while others produce non-unique TOFs. The presumably undesirable combinations $\phi$, $q$, and $N$ where non-unique orbits are possible are described by region $\mathcal{B}$ in Figs. 10 and 11. If velocity geometry lies in $\mathcal{B}$ and we are also given a TOF that happens to fall within the range of ambiguous TOFs, the IOD solution will not be unique (e.g., Fig. 14).

We have yet to determine an analytic expression for the region $\mathcal{B}$. While it is straightforward to find this region numerically (as was done to generate Figs. 10 and 11), determining TOF as a function of $s_k$ requires the evaluation of Kepler's equation. Unfortunately, however, the existing graphical representations of Kepler's equation on the hodograph [3] do not lend themselves to straightforward analysis. Further exploration of the underlying cause of non-uniqueness in $\mathcal{B}$ (or formal guarantees of uniqueness in $\mathcal{A}$) is a topic of ongoing research.

Additional insight into uniqueness may be gained by looking at a few example measurement geometries, denoted by markers A, B, and C in Fig. 10. Measurement geometries such as A and C are in the region where all TOFs correspond to a unique orbit, as can be seen in Figs. 12 and 13. Conversely, measurement geometries such as B have a range of parameter values where the TOF does not correspond to a unique orbit, as shown in Fig. 14. Any TOF in this range could be explained by more than one orbit. Three such orbits are plotted in Fig. 15. To further convince the reader, results for the possible orbits marked in Figs. 14 and 15 are tabulated in Table 2.

As mentioned earlier, we have yet to develop an analytic expression for the region $\mathcal{B}$ containing non-unique solutions. Until such an analytic expression can be developed, we suggest the analyst check for uniqueness by graphically evaluating if the geometry in question lies in region $\mathcal{A}$ or $\mathcal{B}$. Furthermore, while the existence of non-unique solutions in $\mathcal{B}$ is troublesome, it is often straightforward to avoid in
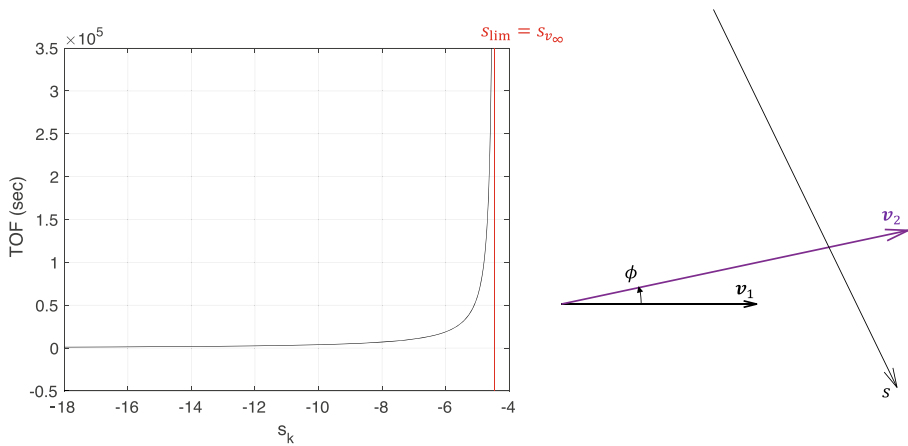
**Fig. 12** TOF plot and hodograph parameterization given velocity vector pair A from Fig. [10]. The TOF monotonically increases with $s_k$. Vectors $v_1$ and $v_2$ are separated by less than 180 deg, so the limit $s_{\text{lim}}$ occurs where $v_1$ becomes the hyperbolic excess velocity

practice. The easiest solution is to acquire one (or more) additional measurements and apply the analytic methods summarized in Table [1] (which has no ambiguities). Alternatively, if truly restricted to only two measurements, select measurement timing to avoid obtaining samples in $\mathcal{B}$.

### Initialization

Our solution to IOD from two velocity vectors and TOF is iterative. Assuming an orbit is expected to be unique for all TOFs (geometry belongs to region $\mathcal{A}$ from
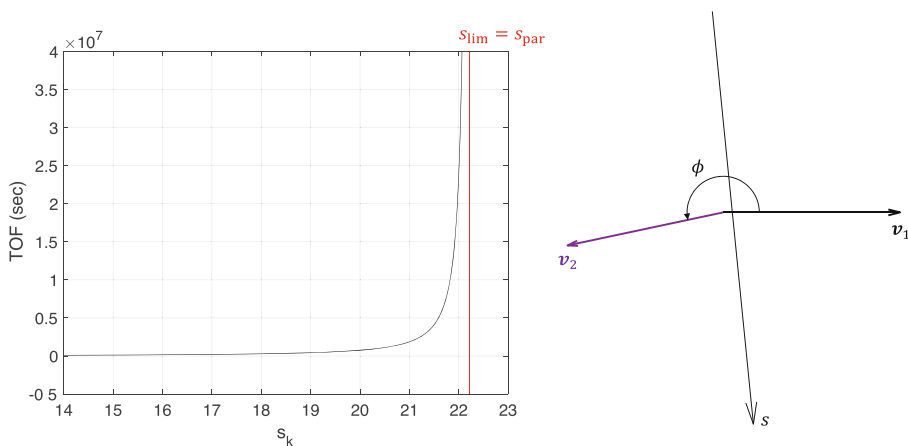


**Fig. 13** TOF plot and hodograph parameterization given velocity vector pair C from Fig. [10]. The TOF monotonically increases with $s_k$. Vectors $v_1$ and $v_2$ are separated by more than 180 deg in the direction of motion, so the TOF approaches infinity at $s_{\text{lim}} = s_{\text{par}}$
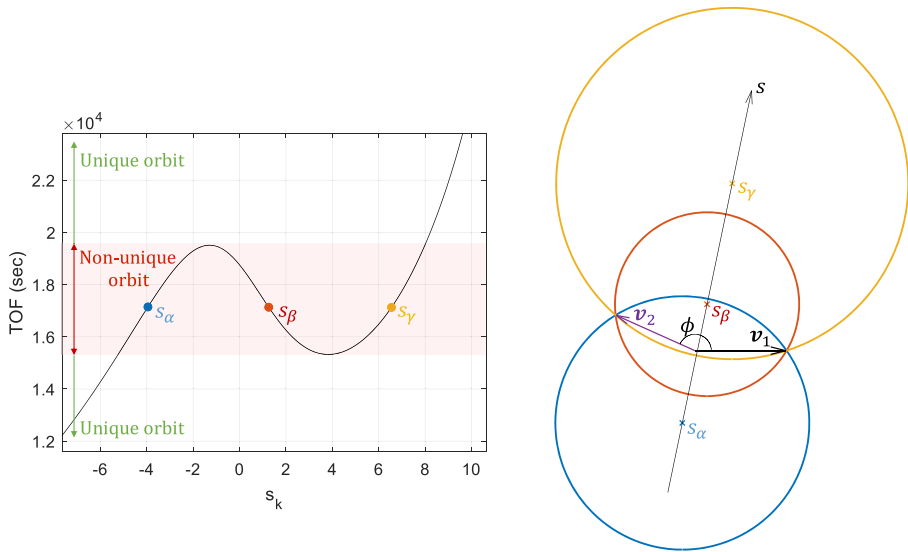
**Fig. 14** Three possible hodograph fits (right) given velocity vector pair B from Fig. 10 produce three distinct orbits where the TOFs (left) from $t_1$ to $t_2$ are equal

Figs. 10 or 11), the next step is to find a good place to initialize the iterative routine within the feasible region for $s_k$ (that is, $s_k < s_{\lim}$). We choose to always initialize with the minimum eccentricity orbit, as this is guaranteed to be a feasible orbit. Because eccentricity is always non-negative, minimizing $e$ is the same as
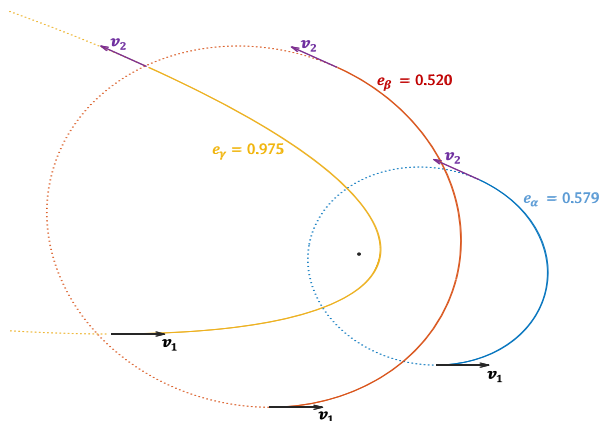


**Fig. 15** Three possible orbits with the same TOF between identical velocity pair $v_1$ and $v_2$. This example corresponds to marker B in Fig. 10 and the hodograph parameterization in Fig. 14. The solid portion of the orbit indicates the path traveled by the spacecraft from $t_1$ to $t_2$, and the dotted portion is the remainder of the orbit fit. All three orbits are elliptical ($e < 1$), with the apoapsis of the gold-colored orbit off the lefthand side of the figure (cropped for clarity)

**Table 2** Orbital Parameters for three orbits shown in Figs. 14 and 15 where $\mu = 3.986 \times 10^5 \text{km}^3/\text{sec}^2$, $\boldsymbol{v}_1 = [1.633581, -3.000775, -1.933415]^T$ km/sec, $\boldsymbol{v}_2 = [-0.118322, 3.387923, 1.542308]^T$ km/sec, and $\Delta t = 17\{,\}144.5$ sec. Extra significant digits are provided to help the reader more reliably reproduce these results

| Orbit | $\alpha$ | $\beta$ | $\gamma$ |
|---|---|---|---|
| $e$ | 0.579407 | 0.519982 | 0.974748 |
| $M_1$ (deg) | 69.59488 | 315.48382 | 354.46414 |
| $M_2$ (deg) | 284.36312 | 49.66098 | 6.29822 |
| $a$ ($\times 10^5$ km) | 0.202783 | 0.351329 | 1.400407 |
| $r_{1_x}$ ($\times 10^4$ km) | −1.047750 | −2.813996 | −2.87192 |
| $r_{1_y}$ ($\times 10^4$ km) | −1.960009 | −0.189634 | 2.478539 |
| $r_{1_z}$ ($\times 10^4$ km) | −0.478030 | 0.960441 | 2.162007 |
| $r_{2_x}$ ($\times 10^4$ km) | 1.904476 | 2.517137 | 1.196031 |
| $r_{2_y}$ ($\times 10^4$ km) | −0.898597 | 1.910728 | 4.369714 |
| $r_{2_z}$ ($\times 10^4$ km) | −1.104205 | −0.089075 | 1.488756 |

minimizing $e^2$. Therefore, substituting Eqs. 32 and 35 into Eq. 16 produces the following optimization problem in terms of the parameter $s_k$:

$$\min_{s_k} e^2 = \left(\frac{c}{R}\right)^2 = \frac{\boldsymbol{c}^T \boldsymbol{c}}{(\boldsymbol{v}_i - \boldsymbol{c})^T (\boldsymbol{v}_i - \boldsymbol{c})} = \frac{(s_k \boldsymbol{m} + \boldsymbol{b})^T (s_k \boldsymbol{m} + \boldsymbol{b})}{(\boldsymbol{v}_i - s_k \boldsymbol{m} - \boldsymbol{b})^T (\boldsymbol{v}_i - s_k \boldsymbol{m} - \boldsymbol{b})} \quad (43)$$

The optimal solution occurs at $\partial e^2 / \partial s_k = 0$. After some simplification, this yields the following quadratic in $s_k$

$$s_k^2 (\boldsymbol{m}^T \boldsymbol{m})(\boldsymbol{m}^T \boldsymbol{v}_i) + s_k \left(2(\boldsymbol{m}^T \boldsymbol{m})(\boldsymbol{b}^T \boldsymbol{v}_i) - (\boldsymbol{m}^T \boldsymbol{m})(\boldsymbol{v}_i^T \boldsymbol{v}_i)\right)$$
$$+ 2(\boldsymbol{m}^T \boldsymbol{b})(\boldsymbol{b}^T \boldsymbol{v}_i) - (\boldsymbol{m}^T \boldsymbol{b})(\boldsymbol{v}_i^T \boldsymbol{v}_i) - (\boldsymbol{b}^T \boldsymbol{b})(\boldsymbol{m}^T \boldsymbol{v}_i) = 0 \quad (44)$$

Because $\boldsymbol{m}$ is a unit vector, this simplifies further to

$$s_k^2 \boldsymbol{m}^T \boldsymbol{v}_i + s_k (2\boldsymbol{b}^T \boldsymbol{v}_i - \boldsymbol{v}_i^T \boldsymbol{v}_i) + 2\boldsymbol{m}^T \boldsymbol{b}\boldsymbol{b}^T \boldsymbol{v}_i - \boldsymbol{m}^T \boldsymbol{b}\boldsymbol{v}_i^T \boldsymbol{v}_i - \boldsymbol{b}^T \boldsymbol{b}\boldsymbol{m}^T \boldsymbol{v}_i = 0 \quad (45)$$

The two roots of the quadratic are

$$s_a = \frac{-B + \sqrt{B^2 - 4AC}}{2A} \quad (46)$$

and

$$s_b = \frac{-B - \sqrt{B^2 - 4AC}}{2A} \quad (47)$$

where

$$A = \boldsymbol{m}^T \boldsymbol{v}_i \quad (48)$$
$$B = 2\boldsymbol{b}^T \boldsymbol{v}_i - \boldsymbol{v}_i^T \boldsymbol{v}_i \quad (49)$$
$$C = 2\boldsymbol{m}^T \boldsymbol{b}\boldsymbol{b}^T \boldsymbol{v}_i - \boldsymbol{m}^T \boldsymbol{b}\boldsymbol{v}_i^T \boldsymbol{v}_i - \boldsymbol{b}^T \boldsymbol{b}\boldsymbol{m}^T \boldsymbol{v}_i \quad (50)$$

One root is the minimum eccentricity hodograph center and the other is the maximum. The second derivative can be used to determine which one corresponds to the

minimum eccentricity, but substituting $s_a$ and $s_b$ into Eqs. 32, 35, and 16 is more computationally efficient. Therefore, the initial parameter is chosen according to

$$s_0 = \begin{cases} s_a, & e(s_a) < e(s_b) \\ s_b, & e(s_a) > e(s_b) \end{cases} \tag{51}$$

The center point and radius of the initial hodograph circle are then given by

$$c_0 = s_0 m + b \tag{52}$$

and

$$R_0 = \|v_i - c_0\| \tag{53}$$

Figure 16 shows an example plot of eccentricity as a function of parameter $s_k$. The minimum and maximum eccentricities for an unconstrained $s_k$ are also shown. In this case, the value of $s_k$ that would maximize eccentricity happens to occur beyond the upper limit $s_{\text{lim}}$ and does not correspond to a physically realizable orbit. Thus, the largest realizable eccentricity occurs at $s_{\text{lim}}$ in this example. It can be seen that the eccentricity asymptotically approaches 1 as $s_k$ becomes increasingly large or small.

## Iterative Method

Beginning with an initial guess of $s_0$ as found from Eqs. 46–51, we seek to iteratively update our estimate of $s_k$ until the current iteration's TOF ($\Delta t_k$) is within a specified tolerance of the true TOF ($\Delta t_{\text{true}}$). There are a number of options for numerical schemes that can be used, but we have found the Newton-Raphson method to be a simple and effective approach for solving this problem.

Unfortunately, direct iteration through evaluation of the TOF residual performs poorly in many cases due to the rapid increase of TOF as $s_k \to s_{\text{lim}}$. We find, however, that the reciprocal of the TOF ($1/\Delta t_k$) behaves in a more benign manner as $s_k$ is changed. This can be seen in Fig. 17. Therefore, iterating on $h(s_k) = 1/\Delta t_k$ allows the method to converge more quickly. At each iteration, $s_k$ is updated according to

$$s_{k+1} = s_k - \frac{h(s_k) - 1/\Delta t_{\text{true}}}{\partial h(s_k)/\partial s_k} \tag{54}$$
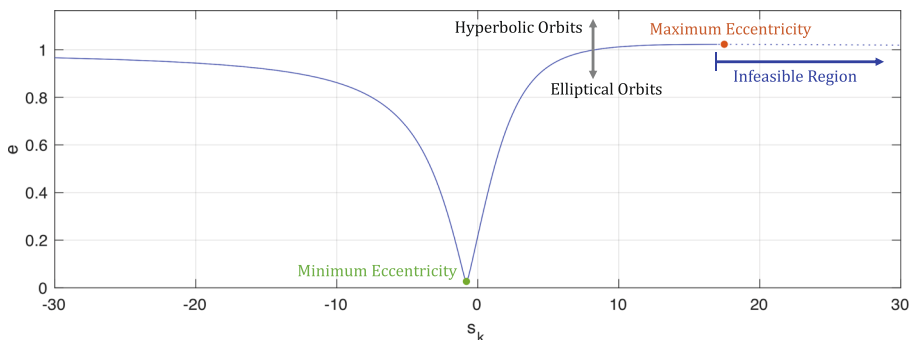


**Fig. 16** Eccentricity as a function of $s_k$ for orbits defined by vector pair B from Figs. 10 and 14. The unconstrained maximum eccentricity occurs in the infeasible region
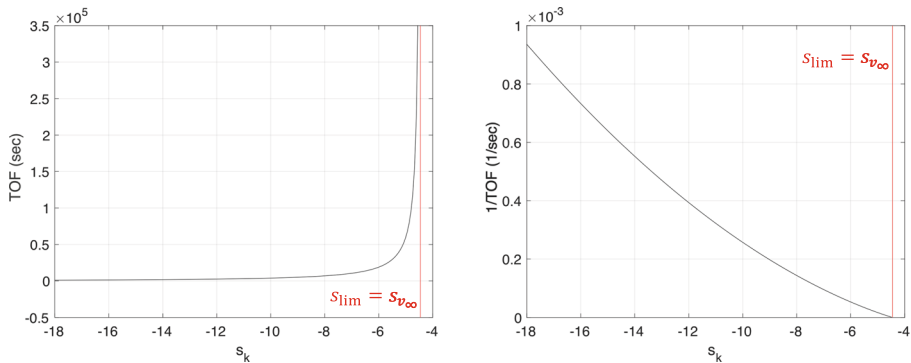
**Fig. 17** Plot of TOF vs. $s_k$ (left) and plot of its reciprocal, 1/TOF, vs. $s_k$ (right) for vector pair A from Figs. 10 and 12. The TOF rapidly increases as $s_k \to s_{\lim}$, but the reciprocal function is more benign

where

$$h(s_k) = \frac{1}{\Delta t_k} \tag{55}$$

and $\partial h(s_k)/\partial s_k$ can be approximated using any appropriate numerical scheme (e.g., finite difference, complex-step).

The newly found $s_k$ may then be used to find the updated hodograph parameters $c_{k+1}$ and $R_{k+1}$

$$c_{k+1} = s_{k+1}m + b \tag{56}$$

$$R_{k+1} = \|v_i - c_{k+1}\| \tag{57}$$

which may, in turn, be used to find the new TOF via Kepler's equation. If the new TOF is within the desired tolerance, stop the iteration. If not, return to Eq. 54 and repeat until convergence.

## Algorithm Summary

A brief summary outlining the solution procedure for performing IOD with two velocity vectors and time-of-flight is provided in Table 3.

## Numerical Results

The velocity-based IOD methods were validated and assessed through a number of numerical studies. These studies are presented in the following subsections.

### Example Orbit Determination with Perfect Measurements

First, the performance of the new IOD methods was evaluated for perfect measurements. Both methods are able to exactly recover the true orbit for any orbit shape (circular, elliptical, parabolic, and hyperbolic) to within machine precision. Some sample cases are provided.

**Table 3** Algorithm summary for IOD from two velocity vectors and time-of-flight

| | |
|---|---|
| Step 1: | Obtain two velocity vectors $\{\boldsymbol{v}_1, \boldsymbol{v}_2\}$, the time-of-flight $\Delta t$, the number of complete revolutions $N$, and specify the direction of motion. |
| Step 2: | Compute the orbital plane normal vector $\boldsymbol{k}$, using Eq. 31 with sign chosen according to the direction of motion. |
| Step 3: | Define the parameterized line through point $\boldsymbol{b}$ with direction $\boldsymbol{m}$ from Eqs. 33 and 34. |
| Step 4: | Compute the parameter bounds from Eq. 41 and determine whether a unique solution exists from Fig. 10. |
| Step 5: | Initialize $\boldsymbol{c}_0$ and $R_0$ using Eqs. 52 and 53. |
| Step 6: | Compute the eccentricity vector $\boldsymbol{e}$ from Eq. 18. |
| Step 7: | Find the direction for each measurement $\boldsymbol{u}_{i\parallel}$ using Eq. 20. |
| Step 8: | Compute $\rho_i$ using Eq. 29. |
| Step 9: | Compute $\boldsymbol{r}_i$ using Eq. 30. |
| Step 10: | Compute the time-of-flight $\Delta t_k$ using Kepler's equation. |
| Step 11: | If $\Delta t_k \not\approx \Delta t_{\text{true}}$, compute $s_{k+1}$ using Eq. 54 and $\boldsymbol{c}_{k+1}$ and $R_{k+1}$ using Eqs. 56 and 57. |
| Step 12: | Repeat Steps 5-10 until $\Delta t_k \approx \Delta t_{\text{true}}$ within a specified tolerance. |

The analytic solution to the IOD problem given three velocity vectors was evaluated using the same scenario presented in [9] for a simulated spacecraft in a prograde Earth orbit undergoing Keplerian motion. The simulated orbit has a perigee radius of 7,178.1 km, inclination of 30 deg, argument of periapsis of 70 deg, and right ascension of the ascending node (RAAN) of 40 deg. The eccentricities vary to create examples of a circular orbit ($e = 0$), an elliptical orbit ($e = 0.4$), a parabolic orbit ($e = 1.0$), and a hyperbolic orbit ($e = 1.2$). Given three velocity measurements placed around the example orbits, the IOD method is used to find the unknown position vectors at the corresponding times. In all cases, the unknown position vectors at all three times are recovered to within machine precision as shown in Table 4.

This same scenario was also used to evaluate the performance of the iterative solution to the IOD problem given two velocity measurements and TOF. The inputs to the algorithm were the velocity vectors and TOF corresponding to times $t_1$ and $t_2$ from Table 4. The TOF tolerance for the iterative method was set to $1 \times 10^{-11}$ sec. Again, the unknown position vectors at both times are recovered to within machine precision as shown in Table 5. Observe that the method converges immediately for circular orbits, as the initial guess is always the lowest eccentricity orbit. Higher eccentricity orbits still converge fairly quickly. For the elliptical orbit ($e = 0.4$), the convergence history is plotted in Fig. 18.

## Performance Assessment Under Measurement Noise

Next, the performance of the IOD methods were evaluated for velocity measurements corrupted by noise. It is important to consider degradation in algorithm performance

**Table 4** IOD-produced position estimates are correct to within machine precision when all three velocity measurements are perfect

| Orbit | Meas. | True | Normalized error | | |
|---|---|---|---|---|---|
| type | time | anomaly | $\delta r_x/\|\mathbf{r}_i\|$ | $\delta r_y/\|\mathbf{r}_i\|$ | $\delta r_z/\|\mathbf{r}_i\|$ |
| Circular | $t_1$ | 20 deg | $3.1676 \times 10^{-16}$ | $-3.8011 \times 10^{-16}$ | $-6.3352 \times 10^{-17}$ |
| ($e = 0.0$) | $t_2$ | 60 deg | $1.1403 \times 10^{-15}$ | $-3.1676 \times 10^{-16}$ | $-3.1676 \times 10^{-16}$ |
| | $t_3$ | 100 deg | $7.6022 \times 10^{-16}$ | $4.4346 \times 10^{-16}$ | $9.5028 \times 10^{-17}$ |
| Elliptical | $t_1$ | 47 deg | $-1.1491 \times 10^{-16}$ | $6.8944 \times 10^{-16}$ | $4.5963 \times 10^{-16}$ |
| ($e = 0.4$) | $t_2$ | 107 deg | $-3.2029 \times 10^{-16}$ | $-2.4022 \times 10^{-16}$ | $1.5014 \times 10^{-17}$ |
| | $t_3$ | 138 deg | $6.3392 \times 10^{-17}$ | $-3.8035 \times 10^{-16}$ | $-3.1696 \times 10^{-16}$ |
| Parabolic | $t_1$ | 37 deg | $-1.1382 \times 10^{-16}$ | $4.5530 \times 10^{-16}$ | $6.8295 \times 10^{-16}$ |
| ($e = 1.0$) | $t_2$ | 80 deg | $-1.1820 \times 10^{-15}$ | $-9.2345 \times 10^{-16}$ | $3.3244 \times 10^{-16}$ |
| | $t_3$ | 100 deg | $-1.5773 \times 10^{-15}$ | $-1.9980 \times 10^{-15}$ | $-1.5773 \times 10^{-16}$ |
| Hyperbolic | $t_1$ | 110 deg | $-3.1122 \times 10^{-15}$ | $-1.8944 \times 10^{-15}$ | $1.2524 \times 10^{-15}$ |
| ($e = 1.2$) | $t_2$ | 129 deg | $-3.9163 \times 10^{-15}$ | $-8.0564 \times 10^{-15}$ | $-1.5945 \times 10^{-15}$ |
| | $t_3$ | 134 deg | $-5.4591 \times 10^{-15}$ | $-1.3427 \times 10^{-14}$ | $-3.5042 \times 10^{-15}$ |

caused by sensor noise, as true measurements are never perfect. Because neither solution method lends itself to a simple expression for the position estimate covariance, the performance was assessed numerically through Monte Carlo simulations.

Monte Carlo analyses were performed using the same simulation scenario previously described, but for an elliptical orbit with eccentricity $e = 0.3$. The mean anomalies of the observations at times $t_1$, $t_2$, and $t_3$ are 36 deg, 144 deg, and 252 deg, respectively. This example orbit and its hodograph fit are plotted in Fig. 19.

**Table 5** IOD-produced position estimates are correct to within the specified iteration tolerance (TOF tolerance: $1 \times 10^{-11}$ sec) when both velocity measurements are perfect

| Orbit | Meas. | True | Iter. | TOF error | Normalized error ($\times 10^{-16}$) | | |
|---|---|---|---|---|---|---|---|
| type | time | anomaly | count | ($\times 10^{-12}$ sec) | $\delta r_x/\|\mathbf{r}_i\|$ | $\delta r_y/\|\mathbf{r}_i\|$ | $\delta r_z/\|\mathbf{r}_i\|$ |
| Circular | $t_1$ | 20 deg | 1 | $-0.2274$ | 3.1676 | $-2.5341$ | $-1.9006$ |
| ($e = 0.0$) | $t_2$ | 60 deg | | | 3.8011 | $-1.2670$ | $-1.2670$ |
| Elliptical | $t_1$ | 47 deg | 5 | 1.8190 | $-1.1491$ | 6.3199 | 3.4472 |
| ($e = 0.4$) | $t_2$ | 107 deg | | | $-1.6015$ | $-4.0036$ | $-1.8016$ |
| Parabolic | $t_1$ | 37 deg | 7 | 0.0000 | 0.0000 | 0.5691 | 0.0000 |
| ($e = 1.0$) | $t_2$ | 80 deg | | | 2.9550 | $-1.4775$ | $-1.4775$ |
| Hyperbolic | $t_1$ | 110 deg | 8 | 2.7285 | 0.0000 | 0.0000 | 4.5112 |
| ($e = 1.2$) | $t_2$ | 129 deg | | | 2.2379 | $-2.2379$ | 1.1189 |
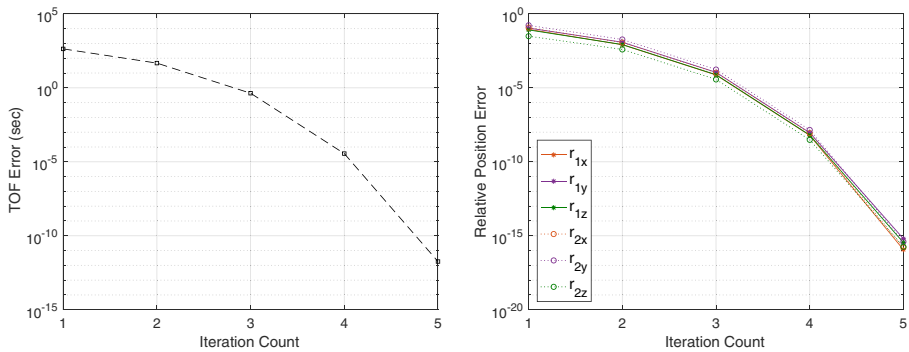
**Fig. 18** Plot of TOF error vs. iteration (left) and relative position error vs. iteration (right) for the elliptical orbit ($e = 0.4$) in Table 5

Velocity measurements were corrupted by noise with a standard deviation of $\sigma_v = 1.0$ m/s. For reference, note that velocity errors on the order of $\sigma_v = 3$ m/s were achieved in [20]. Scatter plots of the IOD-produced position residuals corresponding to the center velocity measurement (at $t_2$) are shown in Fig. 20 for a 1,000-run Monte Carlo where the results generated by the new method (Method 2 - blue ×) are overlayed with the results generated using the algorithm from [9] (Method 1 - black ∘). The IOD produced position errors are nearly identical for both methods. However, the method presented in this paper (Method 2) is algorithmically simpler and requires fewer operations. This difference becomes more significant as the number of velocity measurements increases ($n \geq 4$) because the linear system from Method 1 (Eq. (36) from [9]) scales with $n!$, while the linear system in Eq. 9 scales linearly with $n$.

The iterative two velocity vector IOD method was evaluated with the same scenario (Fig. 19), but using only the velocity vectors at $t_1$ and $t_2$ along with the TOF. Scatter plots of the IOD-produced position residuals corresponding to the velocity
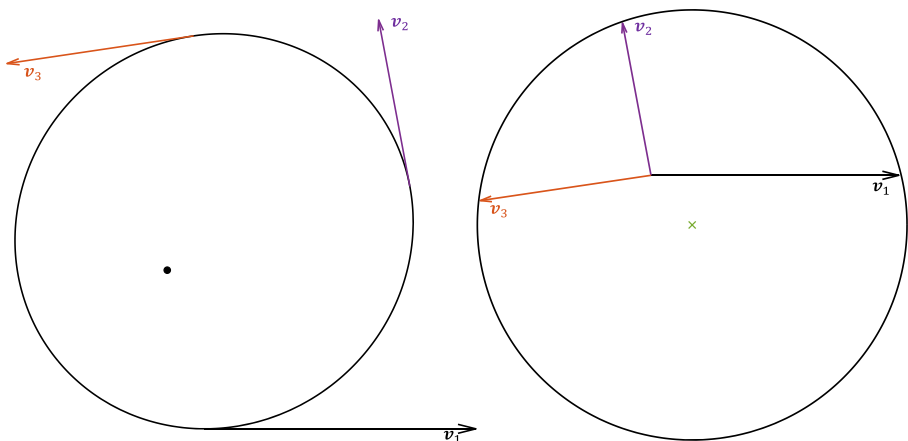


**Fig. 19** Elliptical orbit (left) and hodograph fit (right) of scenario used for Monte Carlo simulations
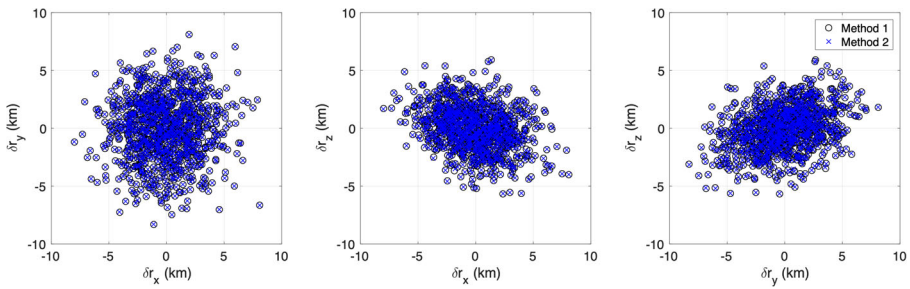
**Fig. 20** Position errors corresponding to center velocity measurement (at $t_2$) for IOD from three velocity measurements. Method 1 (black ○) residuals were produced by the algorithm from [9]. Method 2 (blue ×) residuals were produced by the algorithm described in Section 4. Performance is nearly identical for both methods

measurement at $t_2$ are shown in Fig. 21 for a 1,000-run Monte Carlo. Residuals for this scenario are similar to those in Fig. 20, despite being produced by two velocity vectors and TOF instead of three velocity vectors.

## Performance Degradation as Measurements Become Closer

IOD performance degrades as the velocity measurements become closer to one another. This is a well-known problem for nearly all IOD methods. It is, for example, the primary motivation behind the Herrick-Gibbs modification of the classical Gibbs method [24]. Here, we assess the performance of the three velocity vector IOD method summarized in Table 1 for measurements with angular separation ranging from nearly 0 deg to 10 deg. The test case assumes a circular orbit around Earth with an orbital radius of 7,178.1 km, such that angular separation in true anomaly is always the same as angular separation between the velocity vectors. IOD performance is summarized in Fig. 22 for both perfect measurements and noisy measurements. The perfect measurements show how machine precision affects the proposed IOD scheme when angles become small. We find the relative RMS position error (defined as RMS error normalized by orbital radius) at 10 deg separation is about $10^{-15}$, which is consistent with the double precision arithmetic used to compute these results. The noisy
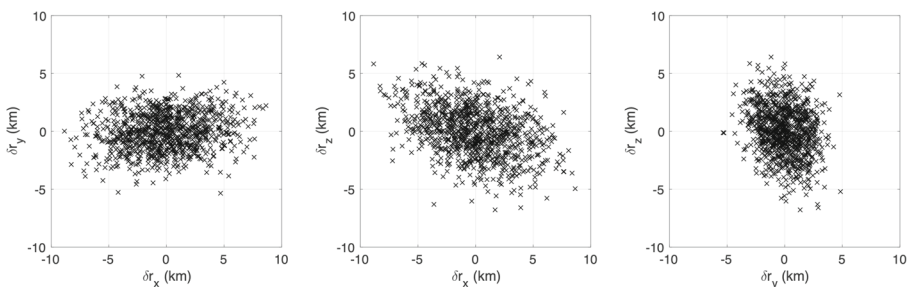


**Fig. 21** Position errors corresponding to second velocity measurement (at $t_2$) for IOD from two velocity vectors and TOF for the same orbit as Fig. 20
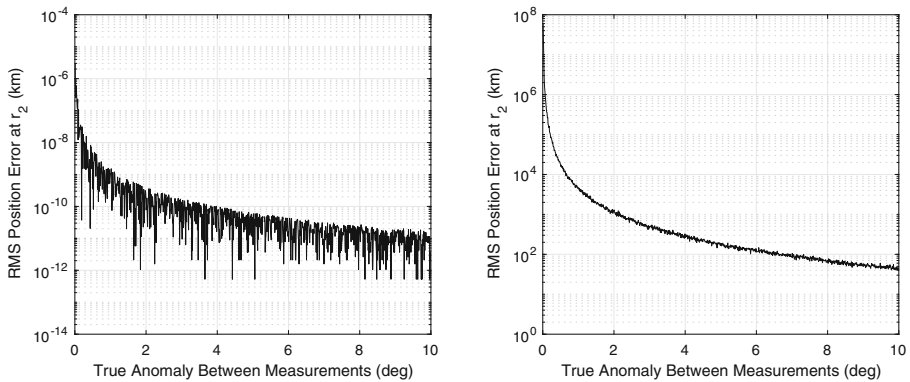
**Fig. 22** The RMS position error increases as the angle between measurements decreases. The occurs for both perfect measurements (left) and noisy measurements (right)

measurements show how IOD performance might degrade in practice. Results for the noisy data were generated via a Monte Carlo analysis with $\sigma_v = 1.0$ m/s.

## Conclusions

This work explores the geometry of initial orbit determination (IOD) given only velocity vector information. Our geometric insights and subsequent analyses are made possible by the orbital hodograph (locus of points traced out by the tip of the trajectory's velocity vector while keeping the tail fixed at the origin), which is known to be a circle for any orbit obeying Keplerian dynamics. We develop novel and straightforward algorithms for IOD given three velocity vectors (a problem first studied in [9]) and IOD given two velocity vectors and time-of-flight (TOF). Observe that the former is the velocity-only analog of the Gibbs problem, while the latter is the velocity-only analog of Lambert's problem. Though the motivation for studying velocity-only IOD originated from X-ray navigation (XNAV), the methods developed in this work are applicable to any future sensor system that directly produces inertial velocity measurements.

The new solution for IOD from three (or more) velocity vectors is non-iterative. In the case of more than three velocity vectors, the optimal orbit fit is found in the least squares sense by direct fitting of the circular hodograph. The new hodograph-based approach presented in this work produces nearly identical IOD solutions as the method from [9] (which is also non-iterative and finds the orbit in the least squares sense), but this new method does so with a simpler algorithm. When compared to [9], our new algorithm requires fewer operations and scales better with an increasing number of measurements.

The new solution for IOD from two velocity vectors and TOF is iterative — just as solutions to Lambert's problem and other variants of the orbital two-point boundary value problem are iterative. This work represents the first known solution (that we're aware of) to IOD with only two velocity vectors and TOF. Our approach reduces

the IOD problem to a single-parameter search for the center of the hodograph circle, which exists somewhere along the perpendicular bisector of the chord connecting the tips of the two known velocity vectors on the hodograph. A unique solution is usually possible, although there are regions where up to three possible orbits could explain the observations. We discuss how the existence of such an ambiguity can be determined from the measurement geometry before even attempting to solve a particular IOD problem. Assuming a unique orbit exists, we suggest initializing the iterative routine at the minimum possible eccentricity orbit (this initial guess may be found analytically). From this starting point, the correct orbit is usually found within a few iterations using a simple gradient-based method.

All velocity-only IOD solution methods presented in this work are shown to find the true orbit to within machine precision when provided noise-free velocity measurements. Algorithms are demonstrated on all classes of two-body orbits (circular, elliptical, parabolic, and hyperbolic) to highlight their generality. Monte Carlo simulations are provided to illustrate how performance degrades as measurement noise is introduced and as measurements become closer together.

## Compliance with Ethical Standards

**Conflict of interests** On behalf of all authors, the corresponding author states that there is no conflict of interest.

## Appendix A: Geometric Properties of the Hodograph

This Appendix explores the relationship between the hodograph and the shape of its corresponding orbit. For clarity, the present discussion is limited to closed orbits. The key observation here is that the perpendicular bisectors of the velocity vectors forming the hodograph circle encapsulate a scaled ellipse of the correct shape that has been rotated by 90 deg. Our discussion of this topic follows the approach of [15]. As a working example, we'll use the hodograph from Fig. 1, which is drawn again in Fig. 23 with a depiction of the encapsulated orbit shape.
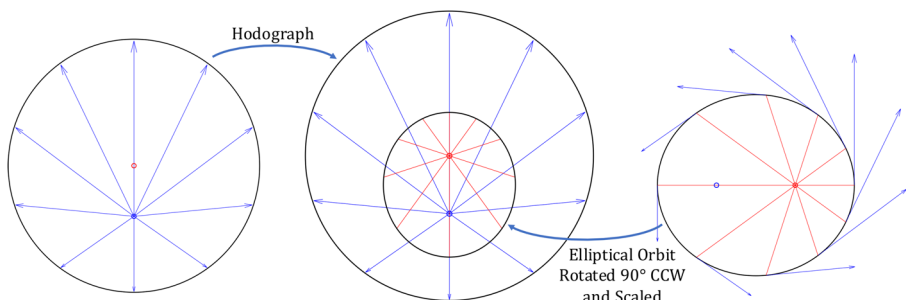


**Fig. 23** Hodograph with encapsulated rotated and scaled elliptical orbit

## A.1 The Circular Hodograph

We begin with a discussion on why the hodograph is always circular. Take the orbit of our working example and divide it into sections of equal angles in true anomaly ($\Delta\theta$), as shown in Fig. 24.

As $\Delta\theta \to 0$ and these segments get very thin, each segment can be approximated as a triangle that has an area proportional to the radius squared. Thus,

$$\Delta A \approx \frac{1}{2}\rho^2 \Delta\theta \qquad (58)$$

which, for a constant $\Delta\theta$,

$$\Delta A \propto \rho^2 \qquad (59)$$

We know from Newton's universal law of gravitation that acceleration, $a$, is proportional to the inverse of the square of the distance

$$a \approx \frac{\|\Delta\boldsymbol{v}\|}{\Delta t} \propto \frac{1}{\rho^2} \qquad (60)$$

We also know from Kepler's Second Law that a constant area is swept out over equal lengths of time

$$\Delta A \propto \Delta t \qquad (61)$$

Substituting Eqs. 59 and 61 into Eq. 60 gives

$$\frac{\|\Delta\boldsymbol{v}\|}{\Delta A} \propto \frac{1}{\Delta A} \qquad (62)$$
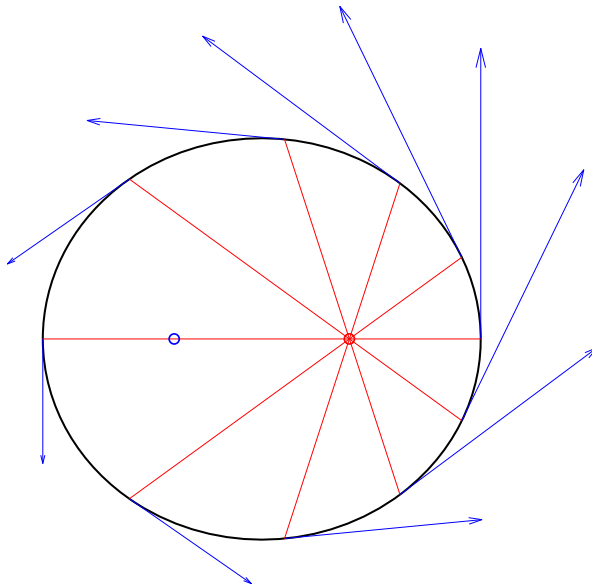


**Fig. 24** Orbit broken into equal-angle segments in true anomaly

which tells us that the magnitude of the change in velocity across each equal-angle segment is constant

$$\|\Delta \boldsymbol{v}\| \propto 1 \tag{63}$$

Likewise, because each successive $\Delta \boldsymbol{v}$ points in the direction of the central body, and each radius changes by a constant $\Delta \theta$, the angular change in velocity is also constant.

Therefore, velocity diagram drawn out by the velocity vectors from equal-angle segments will be a regular polygon which approaches the hodograph circle as the orbit is broken into smaller and smaller segments. This can be seen in Fig. 25.
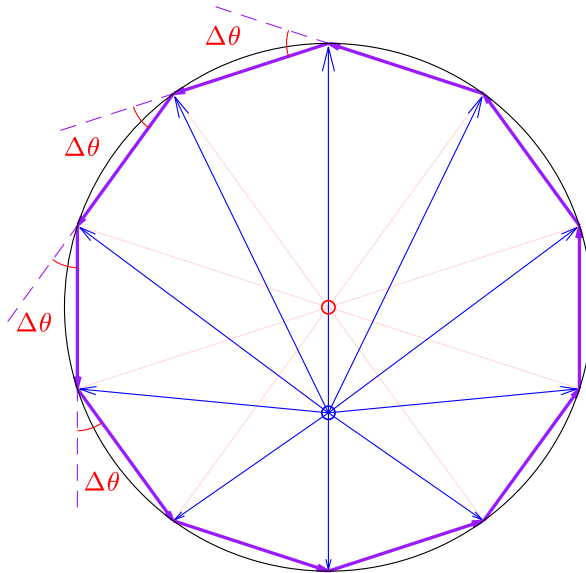


**Fig. 25** Velocity diagram of orbit broken into equal-angle segments is a regular polygon that approaches a circle. External angles $\Delta \theta$ are equivalent to the $\Delta \theta$ of the orbit equal-angle segments

## A.2 Properties of An Ellipse

Take our example hodograph with origin at $O$ and hodograph circle center at $C$. Now, consider one of the velocity vectors belonging to the hodograph (dark blue) and draw its perpendicular bisector (green). Call the tip of the velocity vector point $A$ and the midpoint of this vector point $B$. Now draw the cirle radius connecting $C$ to $A$ (red) and find its intersection point with the perpendicular bisector. Call this point $D$. Now connect points $O$ and $D$ (black dashed), as in Fig. 26.

Notice that triangles $ABD$ and $OBD$ are congruent. Dashed lines $AD$ and $OD$ therefore have equal lengths. This means that the sum of the lengths of lines $OD$ (black dashed) and $CD$ (red solid) is equal to the length of line $AC$, the hodograph radius. This procedure may be repeated for any velocity vector belonging to the orbit, such that $\|OD\| + \|CD\| = R$ around the entire hodograph circle. Thus, the locus
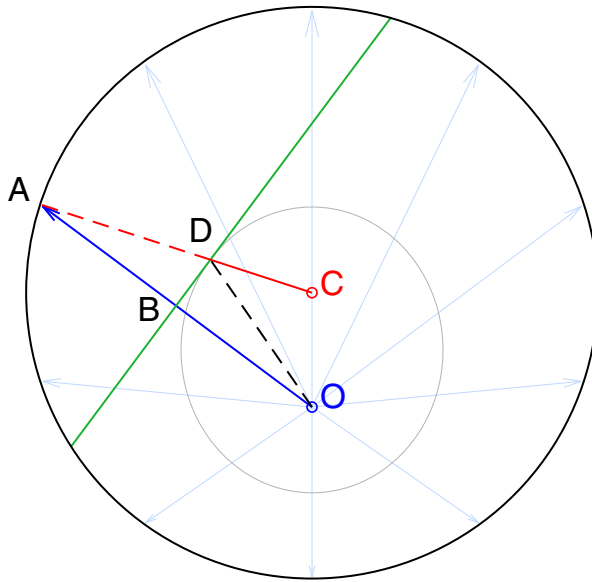
**Fig. 26** Intersection of hodograph radius (red) with perpendicular bisector (green) of velocity vector (blue). Congruent triangles $ABD$ and $OBD$ mean that lines $OD$ and $AD$ have the same length
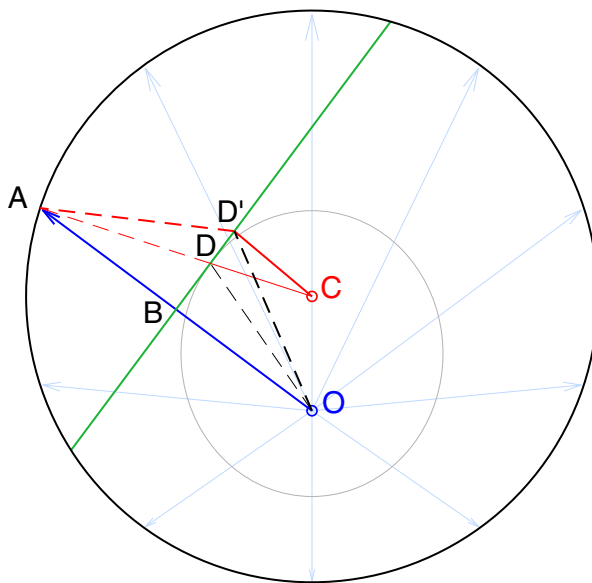


**Fig. 27** The combined distance from origin $O$ and centerpoint $C$ to arbitrary point $D'$ along the perpendicular bisector (green) is greater than the hodograph circle radius

of all points $D$ around the hodograph form an ellipse with focal points $O$ and $C$. The semi-major axis of this ellipse is of length $R/2$.

Also observe that the sum of the distances from $O$ and $C$ to any other point along the perpendicular bisector (green) will be greater than the hodograph radius $\|AC\|$. Take an arbitrary point $D'$ on the perpendicular bisector as shown in Fig. 27. Again, from congruent triangles $ABD'$ and $OBD'$, it is clear that $AD'$ and $OD'$ have equal lengths. Because $D'$ is offset from the line $AC$, the sum of the lengths of $AD'$ and $CD'$ must be greater than the length of line $AC$. Therefore, the sum of the lengths of lines $OD'$ and $CD'$ is greater then the sum of the lengths of lines $OD$ and $CD$ (the major axis of the encapsulated ellipse). Because the sum of distances from the foci to any point on an ellipse is equal to the major axis (a constant), and the sum of the distances from the foci to any other arbitrary point on the perpendicular bisector is greater than the major axis, it follows that all other points $D' \neq D$ on the perpendicular bisector must lie outside the ellipse. Therefore, the perpendicular bisector is tangent to the ellipse at point $D$. This procedure may also be repeated for all velocity vectors belonging to the orbit. The resulting encapsulated ellipse is shown in Fig. 28.
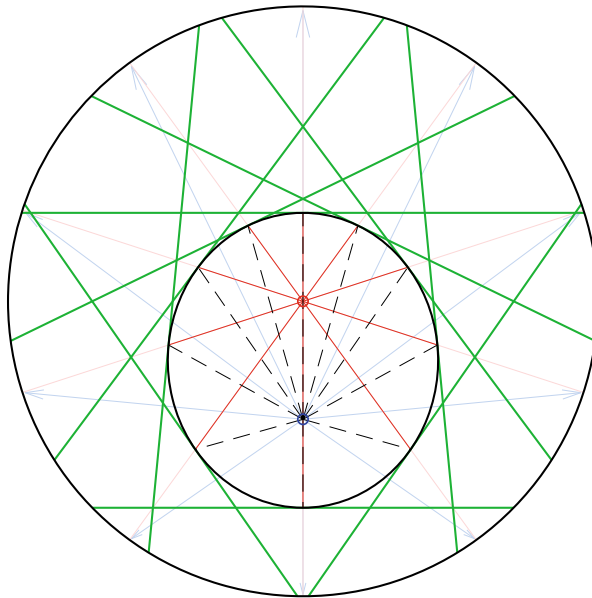


**Fig. 28** The locus of intersection points between velocity vector perpendicular bisectors and corresponding hodograph radii is an ellipse

## A.3 Shape Equivalency between Orbit and Encapsulated Ellipse

Take again our example orbit and hodograph, now shown in Fig. 29 with the orbit rotated 90 deg counter-clockwise. The velocity vector shown on the orbit (blue, left) is of course tangent to the ellipse. It is also parallel to the perpendicular bisector
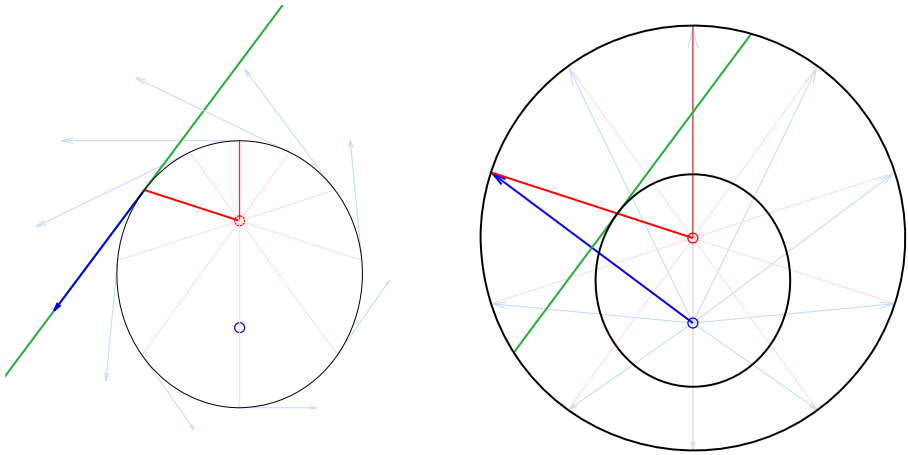
**Fig. 29** Geometric relation between rotated orbit (left) and hodograph (right)

(green), which is tangent to the encapsulated ellipse at the corresponding point. This holds for all velocity vectors. Because the two curves have the same tangent lines at every point, they are equivalent.

Observe that the hodograph circle center (red) corresponds to the central body of the elliptical orbit, while the hodograph origin (blue) corresponds to the empty focus. The radial direction of the orbiting body in the rotated frame is therefore equivalent to the unit vector on the hodograph that points from the hodograph center to the velocity vector tip. This is vector $\boldsymbol{u}_{\perp_i}$, which was shown in Fig. 7. Because the encapsulated ellipse is rotated by 90 deg in the orbit plane, the true radial direction of the orbiting body, $\boldsymbol{u}_{\parallel_i}$, is perpendicular to $\boldsymbol{u}_{\perp_i}$, as described by Eq. 20.

### A.4 Orbit Eccentricity from Hodograph Center and Radius

The relationship between orbit eccentricity and the hodograph shown in Eq. 16 was derived assuming an elliptical orbit. We chose to present the elliptical derivation in the main discussion since it is intuitive and helps develop a better understanding of the problem geometry. In this appendix, we now show that the relation $e = c/R$ developed for elliptical orbits holds for all conic sections.

First, observe that if $c = 0$ then $\|\boldsymbol{v}\| = R$ everywhere on the hodograph. The only way to have a constant speed everywhere on the orbit is to have a circular orbit, thus $e = 0$. Therefore, we observe that $c = 0 \;\rightarrow\; e = 0$, which is certainly satisfied by the relation $e = c/R$. We now turn our attention to all non-circular orbits.

Non-circular orbits occur when the hodograph circle center is offset from the origin (i.e., $c \neq 0$). As observed in Eq. 12, the periapsis velocity magnitude (speed) is given by

$$v_p = R + c \tag{64}$$

where we also observe the periapsis radius is given by

$$r_p = \frac{p}{1+e} \tag{65}$$

where $p$ is the semilatus rectum. Consequently, since velocity is perpendicular to position at the periapsis, the specific angular momentum may be written as

$$h = \frac{p}{1+e}(R+c) \tag{66}$$

Likewise, from Fig. 30, we observe that the component of the velocity vector perpendicular to the position at the semilatus rectum is $R$. Therefore, the specific angular momentum may be written using position and velocity at the semilatus rectum,

$$h = pR \tag{67}$$

Since specific angular momentum is conserved, we may equate Eq. 66 and 67

$$h = \frac{p}{1+e}(R+c) = pR \tag{68}$$

which becomes

$$R + c = R(1+e) \tag{69}$$

or, after simple rearrangement,

$$e = c/R \tag{70}$$

Thus, we have rederived Eq. 16 without making any assumption on the type of conic section. This result is valid for circular, elliptical, parabolic, and hyperbolic orbits.
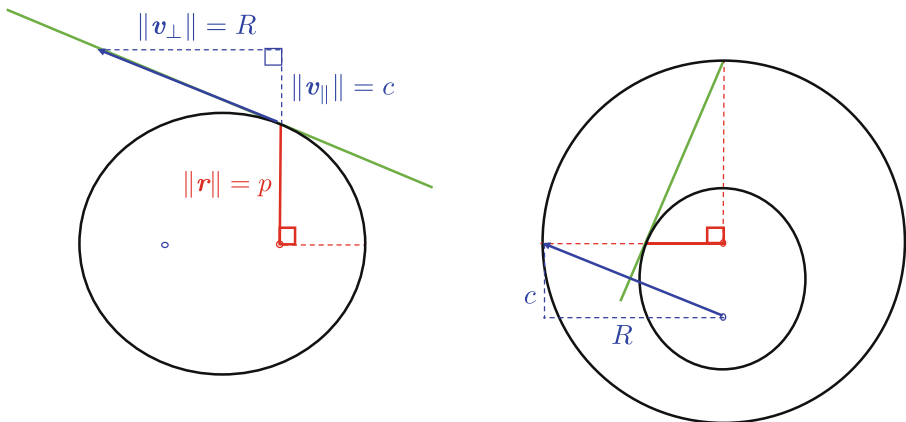


**Fig. 30** Illustration of hodograph geometry when the orbiting body is at the semilatus rectum. Elliptical orbit is shown on the left. Hodograph with encapsulated (rotated and scaled) ellipse on the right

## Appendix B: Hyperbolic Excess Velocity

This appendix demonstrates that the hyperbolic excess velocity $\boldsymbol{v}_\infty$ is tangent to the hodograph circular arc. This geometric relation is derived in two different ways using common expressions for hyperbolic orbits.

**Fig. 31** The hyperbolic excess velocity $\boldsymbol{v}_\infty$ can be expressed in terms of hodograph geometry. This vector forms a right triangle with the vector $\boldsymbol{R}$ where vector $\boldsymbol{c}$ is the hypotenuse
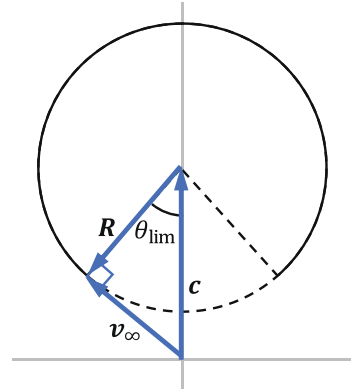
### B.1 From Specific Orbital Energy

Begin with the equation for specific orbital energy

$$\mathcal{E} = -\frac{\mu}{2a} = \frac{v^2}{2} - \frac{\mu}{\rho} \tag{71}$$

where $\rho$ is the range, $\rho = \|\boldsymbol{r}\|$. Expressing Eq. 71 as $\rho \to \infty$

$$\mathcal{E} = -\frac{\mu}{2a} = \frac{v_\infty^2}{2} \tag{72}$$

leads to the relation

$$-\mu = a v_\infty^2 \tag{73}$$

Evaluating Eq. 71 at periapsis

$$\mathcal{E} = \frac{v_p^2}{2} - \frac{\mu}{\rho_p} \tag{74}$$

and substituting Eq. 73 results in

$$\mathcal{E} = \frac{v_p^2}{2} + \frac{a v_\infty^2}{\rho_p} \tag{75}$$

Recall that the radius at periapsis can be found from semi-major axis and eccentricity

$$\rho_p = a(1 - e) \tag{76}$$

so that the specific energy at periapsis becomes

$$\mathcal{E} = \frac{v_p^2}{2} + \frac{a v_\infty^2}{a(1-e)} = \frac{v_p^2}{2} + \frac{v_\infty^2}{1-e} \tag{77}$$

Now, equate this with the specific energy as $\rho$ tends to infinity

$$\mathcal{E} = \frac{v_\infty^2}{2} = \frac{v_p^2}{2} - \frac{v_\infty^2}{1-e} \tag{78}$$

Substituting Eqs. 12 and 16 allows us to express Eq. 78 in terms of parameters that can be directly computed from the hodograph

$$\frac{v_\infty^2}{2} = \frac{(R+c)^2}{2} - \frac{v_\infty^2}{1-\frac{c}{R}} \tag{79}$$

Rearranging this expression, we are left with the Pythagorean Theorem for the right triangle shown in Fig. 31,

$$c^2 = R^2 + v_\infty^2 \tag{80}$$

### B.2 From Limiting True Anomaly

Additionally, we can start with the equation for the limiting true anomaly, $\nu_{\lim}$ from [24]

$$-\pi + \cos^{-1}\left(\frac{1}{e}\right) < \nu < \pi - \cos^{-1}\left(\frac{1}{e}\right) \tag{81}$$

Again, substituting Eq. 16 so that our expression is in terms of hodograph parameters

$$-\pi + \cos^{-1}\left(\frac{R}{c}\right) < \nu < \pi - \cos^{-1}\left(\frac{R}{c}\right) \tag{82}$$

and recognizing that $\theta_{\lim} = \pi - \nu_{\lim}$, we have

$$\theta_{\lim} = \cos^{-1}\left(\frac{R}{c}\right) \tag{83}$$

which also agrees with the right triangle shown in Fig. 31.

## References

1. Al-Sharadqah, A., Chernov, N.: Error analysis for circle fitting algorithms. Electronic Journal of Statistics **3**, 886–911 (2009)
2. Altman, S.: A unified state model of orbital trajectory and attitude dynamics. Celest. Mech. **6**(4), 425–446 (1972)
3. Altman, S.P.: Orbital Hodograph Analysis, vol. 3. American Astronautical Society, Baltimore (1965)
4. Bate, R.R., Mueller, D.D., White, J.E.: Fundamentals of Astrodynamics. Dover Publications, Inc., New York (1971)
5. Battin, R.H.: An Introduction to the Mathematics and Methods of Astrodynamics, Revised Edition. American Institute of Aeronautics and Astronautics, Inc., Reston (1999)
6. Butikov, E.I.: The velocity hodograph for an arbitrary keplerian motion. Eur. J. Phys. **21**(4), 297–302 (2000)
7. Carinena, J.F., Ranada, M.F., Santander, M.: A new look at the feynman 'hodograph' approach to the kepler first law. Eur. J. Phys. **37**(2), 025004 (2016)

8. Carter, T., Humi, M.: Transformed variables and hodographs in impulsive orbit transfer. Acta Astronaut. **123**, 239–245 (2016)

9. Christian, J.A., Hollenberg, C.L.: Initial orbit determination from three velocity vectors. Journal of Guidance, Control, and Dynamics (online ahead of print.) https://doi.org/10.2514/1.G003988

10. Derbes, D.: Reinventing the wheel: Hodographic solutions to the kepler problems. Am. J. Phys. **69**(4), 481–489 (2001)

11. Eades, J.B.: Orbit information derived from its hodograph. In: NASA TM X-63307, X-643-68-264 (1968)

12. Escobal, P.R.: Methods of Orbit Determination, 2nd edn. Robert E. Krieger Publishing Company, Malabar (1976)

13. Gondelach, D., Noomen, R.: Hodographic-shaping method for low-thrust interplanetary trajectory design. J. Spacecr. Rocket. **52**(3), 728–738 (2015)

14. Gooding, R.: A new procedure for the solution of the classical problem of minimal orbit determination from three lines of sight. Celest. Mech. Dyn. Astron. **66**, 387–423 (1997)

15. Goodstein, D.L., Goodstein, J.R.: Feynman's Lost Lecture: The Motion of Planets Around the Sun. W. W. Norton & Company, New York (1996)

16. van Haandel, M., Heckman, G.: Teaching the kepler laws for freshmen. Math. Intell. **31**(2), 40–44 (2009)

17. Hamilton, W.R.: The hodograph, or a new method of expressing in symbolical language the newtonian law of attraction. Proc. R. Ir. Acad. **3**, 344–353 (1847)

18. King, H.C.: The history of the telescope. Charles Griffin & Company ltd (1955)

19. Mahajan, B., Vadali, S.R.: Two-body orbital boundary value problems in regularized coordinates. In: AAS/AIAA Astrodynamics Specialist Conference, ASS 18–310 (2018)

20. Mitchell, J.W., Winternitz, L.B., Hassouneh, M.A., Price, S.R., Semper, S.R., Yu, W.H., Ray, P.S., Wolff, M.T., Kerr, M., Wood, K.S., Arzoumanian, Z., Gendreau, K.C., Guillemot, L., Cognard, I., Demorest, P.: Sextant X-Ray pulsar navigation demonstration: initial on-orbit results. In: AAS Guidance and Control Conference, ASS 18–155 (2018)

21. Russell, R.P.: On the solution to every lambert problem. In: AAS/AIAA Astrodynamics Specialist Conference, ASS 18–456 (2018)

22. Sheikh, S.I., Pines, D.J., Ray, P.S., Wood, K.S., Lovellette, M.N., Wolff, M.T.: Spacecraft navigation using x-ray pulsars. J. Guid. Control. Dyn. **29**(1), 49–63 (2006)

23. Thompson, B.F., Choi, K.K., Piggott, S.W., Beaver, S.R.: Orbital targeting based on hodograph theory for improved rendezvous safety. J. Guid. Control. Dyn. **33**(5), 1566–1576 (2010)

24. Vallado, D.A.: Fundamentals of Astrodynamics and Applications, 3rd edn. Microcosm Press, Hawthorne (2007)